Electron correlation in double photoexcitation of H_2S as studied by H(2p) formation: Comparison with H_2O

Kouichi Hosaka,[1,*] Yutaro Torizuka,[1] Kai Minamizaki,[1] Philipp Schmidt,[2] Andre Knie,[2] Arno Ehresmann,[2]
Takeshi Odagiri,[3] Masashi Kitajima,[1] and Noriyuki Kouchi[1]
[1]*Department of Chemistry, Tokyo Institute of Technology, Meguro-ku, Tokyo 152-8551, Japan*
[2]*Institute of Physics and Center for Interdisciplinary Nanostructure Science and Technology (CINSaT),*
University of Kassel, Heinrich-Plett-Straße 40, D-34132 Kassel, Germany
[3]*Department of Materials and Life Sciences, Sophia University, Chiyoda-ku, Tokyo 102-8554, Japan*

(Received 26 June 2018; revised manuscript received 2 October 2018; published 29 November 2018)

Superexcited states of H_2S have been investigated with determining the cross sections for emission of dispersed and nondispersed atomic fluorescence against the incident photon energy in the range 11–40 eV to address the ionization and excitation of the valence electrons. This method enables us to extract the discrete electronic state from the superposition with continuous electronic states. The cross sections for H(2p) formation have been put on an absolute scale. Ten superexcited states have been found, two in the range 13–15 eV are singly excited $2b_2^{-1}$(mo) states with a single configuration and the other eight states in the range 16–25 eV are doubly excited states with multiple configurations. State-resolved dipole oscillator strengths for H(2p) formation in the photoexcitation of H_2S have been determined. Similar experiments have been performed for H_2O. The state-resolved dipole oscillator strengths for H(2p) formation in the photoexcitation of H_2S are $\sim 10^{-3}$, whereas those in the photoexcitation of H_2O range from $\sim 10^{-3}$ to $\sim 10^{-2}$. It is found that major fragment atoms are H(2p) atoms in the photoexcitation of H_2O and S^* in the photoexcitation of H_2S. The superexcited states of H_2O and H_2S are compared based on the similarity and difference of the electronic structures. It turns out from the comparison that (i) the smaller values of the dipole oscillator strengths for H(2p) formation in the photoexcitation of H_2S are related to the change of the major fragment atoms and (ii) the energy splitting of the doubly excited "$4a_1^{-1}$(mo′)" states of H_2S is enhanced in comparison with that of the doubly excited "$2a_1^{-1}$(mo′)" states of H_2O. This enhancement is caused by the stronger electron correlation in H_2S than in H_2O. The similarity in shape is indicated between the inner valence band and inner shell band in the fluorescence cross sections against the incident photon energy for H_2S and H_2O.

DOI: 10.1103/PhysRevA.98.052514

I. INTRODUCTION

Atomic and molecular doubly excited states, superexcited states of the first kind [1,2], are embedded in the ionization continuum in contrast to excited electronic states below the ionization energy. Because of the superposition of discrete and continuous electronic states, the doubly excited states of molecules are not written as the Born-Oppenheimer products [3,4] and under the local approximation [3,4] the molecular doubly excited states are described with the complex potential energies, of which the imaginary part expresses the autoionization rate. The double photoexcitation dynamics of molecules have thus been attractive subjects of research [4–13]. One of the means to observe doubly excited molecules is determining cross sections for the emission of fluorescence from neutral fragments as functions of excitation energy [7–11,14–30] since the detection of such fluorescence photons, in contrast to the detection of charged species, extracts the discrete electronic state from the superposition with continuous electronic states. Ionization cross section curves show Fano profiles [31] due to the interference between the discrete electronic state and the continuous electronic state on top of the contribution of the uncoupled continuous states and it is hence difficult to extract the contribution of the discrete electronic state alone. The fluorescence cross section curves, however, do not include such interference pattern and the contribution of the discrete electronic state is naturally extracted.

The cross sections for the emission of Lyman fluorescences, H($n \geqslant 2 \to n' = 1$), and Balmer fluorescences, H($n \geqslant 3 \to n' = 2$), were measured in the photoexcitation of the second row hydrides, CH_4 [15,18], NH_3 [16,19], and H_2O [17,20,21] as functions of incident photon energy in the range of the excitation and ionization of outer and inner valence electrons, which is simply referred to as the outer and inner valence range. The outer valence bands show simple features due to the singly excited states with a single configuration, whereas the inner valence bands show complex and broader features comprising a number of peaks due to doubly excited states with multiple configurations. It turned out from the aforementioned investigations on CH_4 [15,18], NH_3 [16,19], and H_2O [17,20,21] that the precursor doubly excited states dissociating into excited hydrogen atoms in the inner valence range are not so amenable to the independent electron model as the precursor superexcited states in the outer valence range. In other words, the electron correlation for the superexcited

---

[*] hosakak@chem.titech.ac.jp

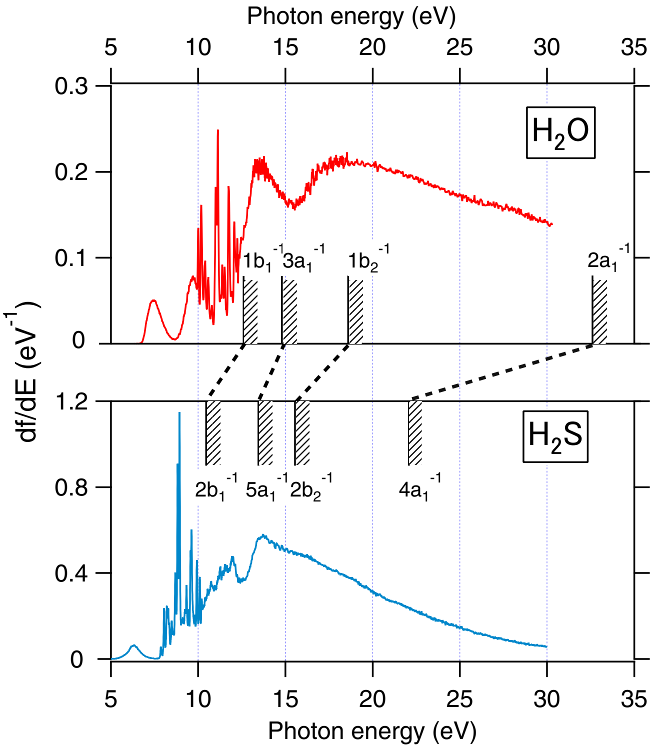

FIG. 1. Densities of the dipole oscillator strengths for the photoabsorption of H_2O [33] and H_2S [34]. Both spectra were recorded with ~50 meV resolution of the incident photon energy. The vertical bars with hatches show the vertical ionization potentials of H_2O [35] and H_2S [36]. The similarity and difference of the electronic structures are seen.

states in the inner valence range is stronger than the electron correlation for those in the outer valence range.

In the present experiment, the superexcited states of the third row hydride H_2S, upon absorption of a single photon, are investigated in the outer and inner valence range. Cross sections for the emission of the Lyman-α fluorescence are determined against the incident photon energy in the range from 11 to 40 eV. The results are compared with the same fluorescence cross sections of H_2O [20] because of the following reasons. Both H_2S and H_2O molecules in their ground electronic states have C_{2v} symmetry and those molecules have eight valence electrons (see the beginning of Sec. IV as well). The electronic structures of them are hence similar, but the electronic structure of H_2S is contracted in comparison with that of H_2O in terms of energy, which is mainly because the valence orbitals in H_2O are dominated by the O $2s$, O $2p$, and H $1s$ orbitals while those in H_2S are dominated by the S $3s$, S $3p$, and H $1s$ orbitals [32]. The similarity and difference between the electronic structures of H_2O and H_2S, in particular the contraction of the electronic structure, are well illustrated in Fig. 1, where the densities of the dipole oscillator strengths for the photoabsorption of H_2O and H_2S are shown against the incident photon energies in the outer and inner valence range [33,34]. The energy gap between the highest outer valence ionized state and inner valence ionized state, i.e., the energy gap between the $1b_2^{-1}/2b_2^{-1}$ state and $2a_1^{-1}/4a_1^{-1}$ state in H_2O/H_2S, respectively, gets remarkably narrower with going from H_2O to H_2S: 14.0 eV for H_2O and 6.5 eV for H_2S as calculated from their vertical ionization potentials (see the beginning of Sec. IV). It is hence expected that the denser population of the superexcited states in H_2S is responsible for the increased electron correlation in the superexcited states of H_2S in the inner valence range, which is mentioned in detail in the beginning of Sec. IV. The comparison between H_2S and H_2O in the present study consequently reveals the influence of the increased electron correlation on molecular superexcited states.

II. EXPERIMENTAL METHODS

In the present experiment we measure the absolute values of cross sections for Lyman-α fluorescence emission in the photoexcitation of H_2S as a function of the incident photon energy in the range 11–40 eV. We carry out the same measurements for H_2O because only the relative cross sections for Lyman-α fluorescence emission were previously measured [20]. In the previous experiment on H_2O the fluorescence photons were detected along the unit polarization vector of the linearly polarized incident light. The angle dependence of the magnitude of the fluorescence emission influences unknowingly the experimental cross sections [37]. For absolute scale measurements of the fluorescence cross sections, photons should be detected at the magic angle as in the present experiment. We use two ways to separate the Lyman-α fluorescence from other fluorescences: the dispersive detection with a grating [21,38] and nondispersive detection with spectral filters [18–20]. The nondispersive detection has the advantage that the detection efficiency is much higher than by the dispersive one, but has the disadvantage that the wavelength resolution is much poorer. For H_2S, as mentioned later, the Lyman-α fluorescence is not dominant (see the dispersed fluorescence spectra in Fig. 2 in Sec. III) in contrast to H_2O. Thus we have skillfully combined the dispersive and nondispersive detections to determine the cross sections for Lyman-α fluorescence emission with a small contamination of other fluorescences and small statistical uncertainty. In the next subsections the experimental details of the dispersive detection is described, followed by those of the nondispersive detection.

A. Dispersed fluorescence experiments of H_2S

The experiments were performed at the 10 m NIM beamline of undulator U125-2 of the Helmholtz-Zentrum Berlin (HZB), i.e., BESSY II [39]. The fluorescence spectra in the photoexcitation of H_2S were measured with an established setup for photon-induced fluorescence spectrometry (PIFS) [21,28,29,38] using a commercial McPherson 1 m normal-incidence spectrometer, which is equipped with a gold-coated 1200 lines/mm grating. The experimental apparatus and procedure for recording the fluorescence spectra is hence described in brief.

The linearly polarized light was introduced into a gas cell fitted to the 1 m normal-incidence spectrometer. We used the H_2S gas sample diluted with He gas because of the consideration for safety: the mole fraction of H_2S is 0.075 and that of He is 0.925. No line of helium atoms is involved

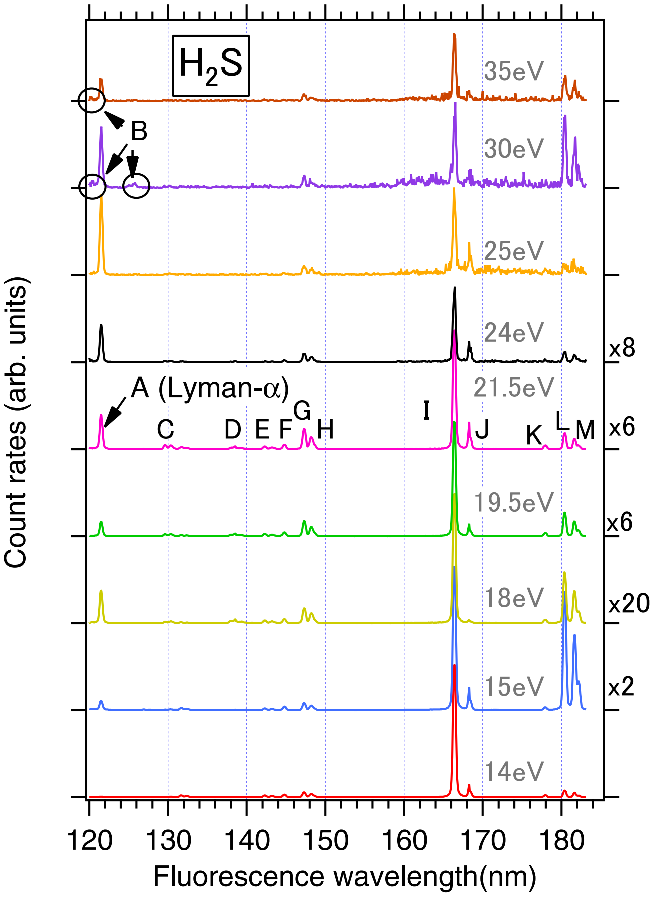

FIG. 2. Dispersed fluorescence spectra in the photoexcitation of H_2S. The energies of the incident photon are shown in the figure. The vertical axis shows the count rate normalized for the total gas pressure and incident photon flux and corrected for the spectral sensitivity of the fluorescence spectrometer including the detector. Each tick on the vertical axis shows a baseline of each spectrum. The vertical scales at energies of 14–24 eV are the same, whereas the vertical scales at energies of 25–35 eV are different from each other and also different from those at energies of 14–24 eV. The labels attached to the peaks are the same as those in Tables I–III and Fig. 3. Line A is the Lyman-α fluorescence and lines C–M are the S^* fluorescence lines while only B is an S^{+*} fluorescence line. Most of the fluorescences detectable by the photon detectors used in the nondispersed fluorescence experiments are included in the figure as mentioned in Sec. II B 1.

in the present range of fluorescence, i.e., 120–185 nm, and excited helium ions are not produced because the maximum photon energy 24 eV is lower than the ionization potential of He atoms (24.59 eV). The total gas pressure in the gas cell was measured with a capacitance manometer and kept within the range so that the fluorescence photon signals are proportional to the total gas pressure, which shows that the quenching of the excited fragment atoms by He atoms or H_2S molecules is ignored. In fact, the total pressure of H_2S was approximately 146 Pa, and the partial pressure of H_2S was thus approximately 11 Pa. The energy of the incident photon was scanned in the range between 12 and 24 eV in 0.5 eV steps. The energy width was 44 meV at 18 eV incident photon energy. The flux of the incident photons was measured with measuring the photocurrent of the last refocusing mirror. The fluorescence emitted perpendicular to the unit polarization vector of the linearly polarized incident light was dispersed by the 1 m normal-incidence spectrometer in the range of the wavelength between 120 and 185 nm at a given incident photon energy, and then the dispersed fluorescence photons were detected with a position sensitive detector composed of a CsTe photocathode, a stack of two microchannel plates (MCPs), and a delay line anode. The count rate for each channel of the position sensitive detector is normalized for the total gas pressure of the sample and incident photon flux and corrected for the sensitivity of the fluorescence spectrometer and detector used in the experiments. The normalized and sensitivity-corrected count rates plotted against the channels, which correspond to the fluorescence wavelengths, give a fluorescence spectrum at a given energy of the incident photon.

B. Nondispersed fluorescence experiments of H_2S and H_2O

The experiments were performed at the bending beamline BL-20A of the Photon Factory, KEK, equipped with a 3 m normal-incidence monochromator [40]. The experimental apparatus is almost the same as that used in our previous study of H_2O [20] and H_2 [9], and is hence described in brief.

Linearly polarized light was introduced into a gas cell filled with sample gas, H_2S, H_2O, or H_2. The H_2 gas was used to put cross sections on an absolute scale. We used pure H_2S gas, not the H_2S gas diluted with He. The pressure in the gas cell was measured with a capacitance manometer and kept within the range so that the fluorescence photon signals are proportional to the sample gas pressure. In fact, the sample gas pressures were approximately 0.5 Pa for H_2S, 0.2 Pa for H_2O, and 0.1 Pa for H_2. The energy of the incident photon was scanned in the range between 11 and 40 eV with 50 meV steps for H_2S, in the range between 13 and 40 eV with 0.1 eV steps for H_2O, and in the range between 25 and 40 eV with 0.2 eV steps for H_2. The bandpass of the incident light was 0.14 nm: the energy width of 100 meV at 30 eV incident photon energy and 50 meV at 21 eV. The flux of the incident photons was measured at the exit of the gas cell using an Au plate, of which sensitivity was calibrated with a silicon photodiode mentioned later. Two photon detectors for vacuum ultraviolet radiation are fitted to the gas cell and are on the plane perpendicular to the incident light beam. Those photon detectors make 54.7° and 234.7° magic angles with respect to the unit polarization vector of the incident light. Angle-integrated cross sections are thereby measured regardless of the fluorescence angular anisotropy. The count rates from the photon detectors were recorded with scanning the incident photon energy.

1. Separation of Lyman-α fluorescence

Each photon detector consists of a 1-mm-thick MgF_2 window and an MCP. The MgF_2 window is used so that charged particles and photons of which wavelength is shorter than approximately 115 nm are not detected (the wavelength of the Lyman-α fluorescence is 121.6 nm). Au-coated tungsten meshes are put on both sides of the MgF_2 window to prevent charging and a leak of the electric field from the MCP. There still remains, however, a small possibility that the stray electric field quenches metastable H(2*s*) atoms through Lyman-α

TABLE I. Detection efficiencies of the CsI-uncoated and coated MCPs [44] for the strong lines in Fig. 2. The enhancement factors of the MCP efficiency, the efficiency of the coated MCP/the efficiency of the uncoated MCP, are also shown in square brackets.

Label[a]	Wavelength (nm)	Uncoated MCP (%)	Coated[b] MCP (%)	Coated[c] MCP (%)
A	121.6	1.5	13[×9]	20[×13]
G, H	148	0.15	20[×130]	30[×200]
I, J	168	0.02	7[×350]	10[×500]
L, M	182	<0.01	4	6
	200	<0.01	0.3	0.7

[a] The labels identify the peaks in Fig. 2 and the excitation spectra in Fig. 3. Label A denotes the Lyman-α fluorescence.

[b] 100-nm-thick coating.

[c] 350-nm-thick coating.

fluorescence emission because H(2s) and H(2p) atoms are likely to be produced from the same precursor superexcited states as shown in the photoexcitation of H_2 [12], CH_4 [41], and NH_3 [41]. The contribution of fragment H(2s) atoms to the Lyman-α photon signal seems to be negligibly small in the present experiment because, as seen in Fig. 4, the cross section curve for H(2p) formation from H_2 obtained in the present experiment (open green circles) is in agreement with that independently reported by [42] (open blue triangles) in terms of shape, and the comparable number of H(2s) atoms are produced from H_2 in addition to H(2p) atoms in this range of the incident photon energy [12].

The photon detectors are operated simultaneously so as to separate the Lyman-α fluorescence from the signals due to other fluorescences in the photoexcitation of H_2S: one of the detectors incorporates an MCP coated with CsI and the other incorporates an MCP without coating [43,44], and the detection efficiencies of those MCPs are hence different. The difference in the detection efficiencies of those two types of MCPs play a major role in separating the Lyman-α fluorescence as mentioned in detail below.

In Table I the detection efficiencies of the MCPs with and without CsI coating [44] are shown for the prominent lines in the fluorescence spectra in the photoexcitation of H_2S shown in Fig. 2 (see Sec. III). It is clearly seen that the CsI-coated MCP enhances the detection efficiency, in particular in the range of the wavelength longer than 150 nm. The enhancement factors of the MCP efficiency, the ratios of the efficiency of the coated MCP to that of the uncoated MCP, are also shown in square brackets in Table I. It turns out from Fig. 2 that even signals from the photon detector incorporating the MCP without CsI coating are not dominated by the Lyman-α fluorescence in the photoexcitation of H_2S. However, taking advantage of the large difference between the detection efficiency of the MCP with CsI coating and that of the MCP without coating (see Table I), the Lyman-α fluorescence is separated from the signals due to other fluorescences in the longer wavelength range in the H_2S experiments, lines G, H, I, J, L, and M in Fig. 2. The range 115–120 nm is involved in our filter range, i.e., the wavelength range longer than 115 nm, but is not involved in the dispersed fluorescence spectra in the photoexcitation of H_2S (see Fig. 2). Following Ref. [45] no fluorescence lines were observed in the range 115–120 nm in the fluorescence spectrum in 100 eV electron collision with H_2S, which is likely to be the case in the photoexcitation of H_2S as well. In contrast to the photoexcitation of H_2S, only the Lyman-α fluorescence is detected in the photoexcitation of H_2 and H_2O as mentioned later.

The enhancement factor of the MCP efficiency for the Lyman-α fluorescence (121.6 nm) was measured in the H_2 experiment as a first step for the separation of the Lyman-α fluorescence, and the result was 5.6, which is 60% of the literature value for an MCP with 100-nm-thick CsI coating in Table I. This decrease is probably because the efficiency of the CsI-coated MCP is less stable than that of the uncoated MCP, due to the deliquescence of CsI. The enhancement factors of the MCP efficiency in the range of the longer wavelength may have been lowered more. In the photoexcitation of H_2 in the present range of the incident photon energy, i.e., 25–40 eV as mentioned, doubly excited H_2 molecules are produced and decay through autoionization and neutral dissociation. Only the Lyman-α fluorescence was hence detected by the present photon detector. The Lyman-β fluorescence at 102.5 nm does not penetrate the 1-mm-thick MgF_2 window as well as other Lyman fluorescence lines. Balmer fluorescences are in the visible range. The ratio of the detection efficiency of the photon detector incorporating the MCP with CsI coating to the efficiency of that without CsI coating could thus be measured experimentally for the Lyman-α fluorescence. The efficiency of the photon detector is the product of the transmittance of the Au-coated tungsten meshes, the transmittance of the MgF_2 window, the detection efficiency of the MCP, and the fraction of the pulses that pass through the discriminator in our counting system. The transmittance of meshes and that of the MgF_2 window do not depend on whether the MCP is coated or not, and the fraction of pulses passing through the discriminator does not depend significantly on whether coated or not if the high voltage applied to the MCP and the threshold of the discriminator are set properly. The measured ratio of the detection efficiencies of the two photon detectors, 5.6, is approximately equal to the enhancement factor of the MCP efficiency for the Lyman-α fluorescence due to the CsI coating.

The count rate for the fluorescence α by the MCP with CsI coating $\dot{N}^{\alpha}_{w}(E)$ and that by the MCP without CsI coating $\dot{N}^{\alpha}_{\mathrm{wo}}(E)$ at a given energy of the incident photon E is related to the cross section for the emission of the fluorescence α differential with respect to the solid angle of emitted photons at the magic angle $q_{\alpha}(E)$ as

$$\begin{aligned}
\dot{N}^{\alpha}_{w}(E) &= n\left(\frac{I'(E)G}{A}\right)\eta^{\alpha}_{w}\langle q_{\alpha}\rangle(E),\\
\dot{N}^{\alpha}_{\mathrm{wo}}(E) &= n\left(\frac{I'(E)G}{A}\right)\eta^{\alpha}_{\mathrm{wo}}\langle q_{\alpha}\rangle(E),
\end{aligned}\tag{1}$$

where $\langle q_{\alpha}\rangle(E)$ is the angle-differential cross section $q_{\alpha}(E)$ convoluted with the angular resolution, n is the number density of target molecules, $I'(E)$ is the flux of the incident photons, A is the cross-section area of the incident photon beam, G is the geometric factor, and η^{α}_{w} and $\eta^{\alpha}_{\mathrm{wo}}$ are the detection efficiencies of the photon detectors incorporating the MCPs with and without CsI coating, respectively, for the fluorescence α. The value of q_α depends on the direction of the emitted fluorescence photon α as well as E. The direction, however, is fixed to the magic angle in the present experiment. The angle-differential cross section q_α is hence a function of only E. The detection efficiencies η^α_w and $\eta^\alpha_{\rm wo}$ are the products of the transmittance of the metal meshes, the transmittance of the 1-mm-thick $\mathrm{MgF_2}$ window for the fluorescence α, the detection efficiency of the MCP for the fluorescence α, and the fraction of the pulses that pass through the discriminator. The factors G and A are independent of E, since the position and shape of the incident light beam does not change significantly with scanning E. The MCPs with and without CsI coating were operated simultaneously.

In the nondispersed fluorescence experiments, the observed signal is the summation of $\dot{N}^\alpha_w\,(E)$ and $\dot{N}^\alpha_{wo}\,(E)$ in Eq. (1) over fluorescence α:

$$\dot{N}_w(E) = \sum_\alpha \dot{N}^\alpha_w(E),$$
$$\dot{N}_{\rm wo}(E) = \sum_\alpha \dot{N}^\alpha_{\rm wo}(E), \tag{2}$$

where the fluorescence α runs in the fluorescence wavelength range between 115 and 200 nm. The cutoff at 115 nm is determined by the $\mathrm{MgF_2}$ window and the cutoff at 200 nm is determined by the MCP (see Table I). The variable α in Eq. (2) starts with the Lyman-α fluorescence line because line B, the $\mathrm{S^{+*}}$ fluorescence as mentioned in Sec. III A, is much weaker than the Lyman-α fluorescence (see Fig. 2) and no fluorescence lines were observed in the range 115–120 nm in 100 eV electron collision with $\mathrm{H_2S}$ [45], and then the variable α further extends to the cutoff at 200 nm via prominent $\mathrm{S^*}$ fluorescence lines (G, H, I, J, L, and M in Fig. 2). We hence divide the summation in Eq. (2) into two terms, i.e., the Lyman-α term and the term of other fluorescences at longer wavelengths:

$$\dot{N}_w(E) = n\left(\frac{I'(E)G}{A}\right)\left\{\eta^H_w\langle q_H\rangle(E) + \sum_\beta \eta^\beta_w\langle q_\beta\rangle(E)\right\}, \tag{3}$$

$$\dot{N}_{\rm wo}(E) = n\left(\frac{I'(E)G}{A}\right)\left\{\eta^H_{\rm wo}\langle q_H\rangle(E) + \sum_\beta \eta^\beta_{\rm wo}\langle q_\beta\rangle(E)\right\}. \tag{4}$$

In Eqs. (3) and (4), $\eta^H_{w/\rm wo}\langle q_H\rangle(E)$ is the Lyman-α term and $\sum_\beta \eta^\beta_{w/\rm wo}\langle q_\beta\rangle(E)$ is the term of other fluorescence lines at longer wavelengths. The index H denotes the Lyman-α fluorescence.

The flux of the incident photons $I'(E)$ is related to the photocurrent of the Au plate $i_{\rm Au}(E)$ as

$$I'(E) = CK(E)i_{\rm Au}(E), \tag{5}$$

where C is a constant independent of E. The function $K(E)$, which is related to the sensitivity of the Au plate as a function of the incident photon energy, is obtained with successive measurements of photocurrents of the Au plate and the silicon photodiode (model AXUV-100G, IRD Inc.). The sensitivity of the latter was calibrated by NIST. Because the sensitivity of the silicon photodiode decreased under irradiation of the incident light and the sensitivity of the Au plate was stable, the flux of the incident photons was measured using not the silicon photodiode but the Au plate. The silicon photodiode was used to calibrate the sensitivity of the Au plate.

The count rates $\dot{N}_w$ and $\dot{N}_{\rm wo}$ recorded experimentally are normalized for the target gas pressure P and flux of the incident photons $K(E)i_{\rm Au}(E)$ in Eq. (5):

$$S_w(E) = \frac{\dot{N}_w(E)}{P[K(E)i_{\rm Au}(E)]} = B\left\{\eta^H_w\langle q_H\rangle(E) + \sum_\beta \eta^\beta_w\langle q_\beta\rangle(E)\right\}, \tag{6}$$

$$S_{\rm wo}(E) = \frac{\dot{N}_{\rm wo}(E)}{P[K(E)i_{\rm Au}(E)]} = B\left\{\eta^H_{\rm wo}\langle q_H\rangle(E) + \sum_\beta \eta^\beta_{\rm wo}\langle q_\beta\rangle(E)\right\}. \tag{7}$$

Here B is equal to $[N_A/(RT)][(CG)/A]$, where N_A is the Avogadro's number, R is the gas constant, T is the absolute temperature of the sample gas, and B is hence a constant independent of E and fluorescence α. The large difference between η^β_w and $\eta^\beta_{\rm wo}$ in Eqs. (6) and (7) (see Table I) enables us to separate the Lyman-α term $B\eta^H_w\langle q_H\rangle(E)$ from the term of other fluorescences in the longer wavelength range $B\sum_\beta \eta^\beta_w\langle q_\beta\rangle(E)$. The quantity $S_{\rm wo}(E)$ is multiplied by the factor f^H, which is defined as $f^H = \eta^H_w/\eta^H_{\rm wo}$, to obtain Eq. (8):

$$S_{\rm wo}(E)f^H = B\left\{\eta^H_w\langle q_H\rangle(E) + f^H\sum_\beta \eta^\beta_{\rm wo}\langle q_\beta\rangle(E)\right\}. \tag{8}$$

As mentioned before the value of f^H was measured in this experiment to be $f^H = 5.6$, and is approximately equal to the enhancement factor of the MCP efficiency for the Lyman-α fluorescence. We subtract Eq. (8) from Eq. (6) on both sides to cancel the Lyman-α term in Eq. (6) and the result is

$$\begin{aligned} S_w(E) - S_{\rm wo}(E)f^H &= B\sum_\beta \left(\eta^\beta_w - \eta^\beta_{\rm wo}f^H\right)\langle q_\beta\rangle(E) \\ &= B\sum_\beta \eta^\beta_w\,(1 - f^H/f^\beta)\,\langle q_\beta\rangle(E) \\ &= Ba\sum_\beta \eta^\beta_w\langle q_\beta\rangle(E), \end{aligned} \tag{9}$$

where $f^\beta = \eta^\beta_w/\eta^\beta_{\rm wo}$ is approximately equal to the enhancement factor of the MCP efficiency for the fluorescence β. In obtaining Eq. (9), we use the fact that $(1 - f^H/f^\beta)$ only weakly depends on β and is close to unity since the value of f^H/f^β is much smaller than unity as shown in Table I. The factor of $(1 - f^H/f^\beta)$ is hence replaced by a β-independent factor "a" slightly smaller than unity.

The relative values of $\langle q_H\rangle(E)$ as a function of E are obtained from Eqs. (6) and (9),

$$B\eta_w^H\langle q_H\rangle(E) = S_w(E) - \frac{1}{a}\{S_w(E) - S_{\text{wo}}(E)f^H\}. \qquad (10)$$

The second term of the right-hand side of Eq. (10) equals $B\sum_\beta \eta_w^\beta\langle q_\beta\rangle(E)$, the contribution of the S* fluorescences. The value of a was determined experimentally such that the value of $\langle q_H\rangle(E)$ becomes zero in the range of E below 14.09 eV, the lowest dissociation limit for the formation of H($2p$) atoms (see Table III in Sec. III), and the result was $a = 0.77$. The obtained value of a is slightly smaller than unity as expected. We note that $\langle q_H\rangle(E)$ is approximated by $\sigma_{\text{H}(2p)}(E)/(4\pi)$, where $\sigma_{\text{H}(2p)}(E)$ is the cross section for the formation of H($2p$) atoms, because of the magic angle and the fact that all H($2p$) atoms emit Lyman-α fluorescence. In Sec. III B the present procedure for the separation is justified by comparing the $\sigma_{\text{H}(2p)}(E)$ vs E curve obtained following Eq. (10) in the photoexcitation of H_2S with the excitation spectrum of the Lyman-α fluorescence in Fig. 3 obtained with the dispersed fluorescence experiments of H_2S.

In the photoexcitation of H_2O, we conclude that the photon signal is dominated by the Lyman-α fluorescence because of the following reason. Nakano *et al.* [20] measured the relative values of the cross sections for the emission of the Lyman-α fluorescence in the photoexcitation of H_2O as a function of the incident photon energy in the range 14–60 eV. They measured the cross section curve with the CsI-uncoated MCP incorporating an MgF_2 window. After that Hans *et al.* [21] measured the absolute values of the cross sections for the emission of the Lyman-α fluorescence in the photoexcitation of H_2O in the range 15–34 eV with the same setup as used in the present dispersed fluorescence experiments. The two cross section curves are in agreement with each other in terms of shape [21]. We thus conclude that the Lyman-α fluorescence is dominant in the photoexcitation experiment of H_2O by Nakano *et al.* [20]. In the photoexcitation experiments of H_2O in the range of the valence excitation, $S_w(E)$ is hence related to only $\langle q_H\rangle(E)$ as

$$S_w(E) = B\eta_w^H\langle q_H\rangle(E). \qquad (11)$$

As mentioned in Eqs. (6) and (7), B is a constant independent of E and fluorescence α. Furthermore, B is independent of the sample gas.

The relative values of $\langle q_H\rangle(E)$ are obtained against the incident photon energy E in the photoexcitation of H_2S and H_2O following Eqs. (10) and (11), respectively. In the next subsection we describe the method for determining the absolute values of $\sigma_{\text{H}(2p)}(E)$ in the photoexcitation of H_2S and H_2O.

2. *The method for determining the absolute cross sections for the formation of H(2p) atoms*

We need the value of $B\eta_w^H$ to experimentally determine the values of $\langle q_H\rangle(E)$ for H_2S following Eq. (10) and those for H_2O following Eq. (11). However, it is difficult to measure the value of $B\eta_w^H$. The reference measurement is hence carried out for H_2 since Eq. (11) is valid in the double photoexcitation experiments of H_2 as mentioned in the part of measuring the enhancement factor of the MCP efficiency for the Lyman-α fluorescence and the absolute values of the cross sections for the formation of H($2p$) atoms were reported in the double photoexcitation of H_2 [42].

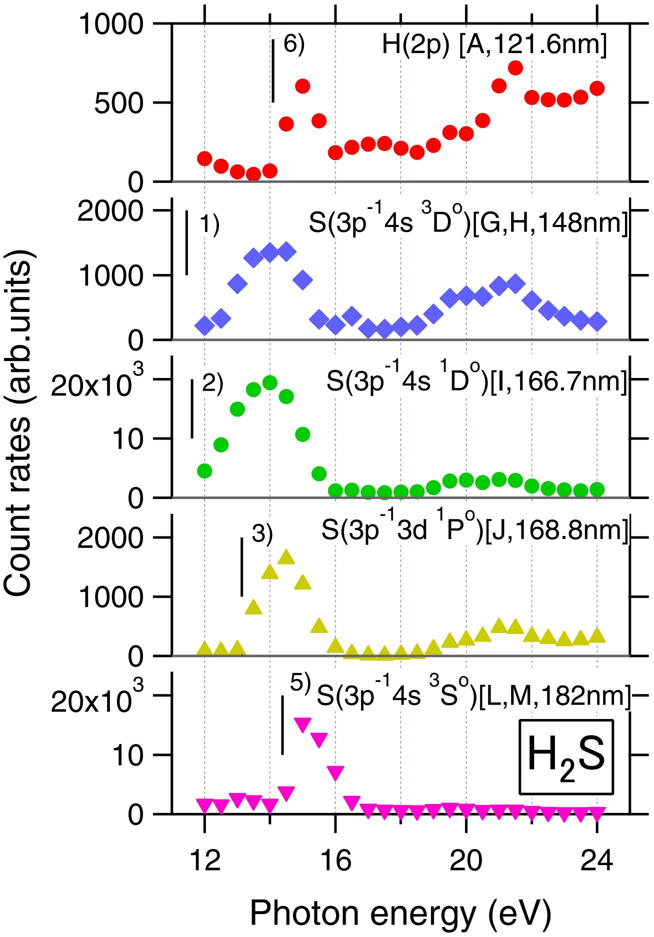

FIG. 3. Excitation spectra for the emission of the fluorescences observed in Fig. 2 in the photoexcitation of H_2S. They are the sum of the normalized count rates over the range of each line in Fig. 2 plotted against the incident photon energy. The alphabetical labels are the same as those in Fig. 2 and Tables I–III. The vertical bars accompanied by the numerical labels show the dissociation limits for the formation of each fluorescent atom in Table III (the numerical labels are the same as those in Table III).

The experiment for H_2S [Eq. (10)] was accompanied by the reference experiment for H_2 [Eq. (11)] and the experiment for H_2O [Eq. (11)] was also accompanied by the reference experiment for H_2 [Eq. (11)]. The values of B and η_w^H were considered unchanged during the successive measurements for H_2S (H_2O) and H_2. Both $B\eta_w^H\langle q_H^{\text{H}_2\text{S}}\rangle(E)$ and $B\eta_w^H\langle q_H^{\text{H}_2}\rangle(E)$ were consequently put on the same relative scale of the vertical axis, and $B\eta_w^H\langle q_H^{\text{H}_2\text{O}}\rangle(E)$ and $B\eta_w^H\langle q_H^{\text{H}_2}\rangle(E)$ were also put on the same relative scale of the vertical axis. The notation of $\langle q_H^{\text{H}_2\text{S}}\rangle(E)$, $\langle q_H^{\text{H}_2\text{O}}\rangle(E)$, and $\langle q_H^{\text{H}_2}\rangle(E)$ would be trivial. The angle-differential cross section $\langle q_H\rangle(E)$ multiplied by 4π is equal to the angle-integrated cross section for the formation of H($2p$) atoms, $\sigma_{\text{H}(2p)}(E)$, as mentioned before. Normalizing the relative values of $\sigma_{\text{H}(2p)}^{\text{H}_2}(E)$ to the absolute ones reported by [42], which corresponds to the experimental determination

TABLE II. Lines observed in the fluorescence spectra in the photoexcitation of H_2S in Fig. 2. The lines are assigned following the results of the electron collision experiment on H_2S [45]. The ground electronic state of an S atom is $1s^22s^22p^63s^23p^4\ {}^3P^e_2$ and that of an S^+ ion is $1s^22s^22p^63s^23p^3\ {}^4S^o_{3/2}$ [46]. The electron configurations of S atoms and S^+ ions are omitted when they are in the electronic states resulting from the ground configurations. Strong lines in the fluorescence spectra in the photoexcitation of H_2S in Fig. 2 are underlined.

Label[a]	Wavelength (nm)	Transition
B	120.4	$S^+(3s^{-1}3p\,{}^2D) \rightarrow S^+({}^2D^o)$
$\underline{\text{A}}$	121.6	$H(2p) \rightarrow H(1s)$
B	125.1	$S^+(3s^{-1}3p\,{}^4P) \rightarrow S^+({}^4S^o)$
B	125.4	$S^+(3s^{-1}3p\,{}^4P) \rightarrow S^+({}^4S^o)$
B	126.0	$S^+(3s^{-1}3p\,{}^4P) \rightarrow S^+({}^4S^o)$
C	129.4	$S(3p^{-1}4s\,{}^3P^o) \rightarrow S({}^3P)$
C	130.2	$S(3p^{-1}4s\,{}^3P^o) \rightarrow S({}^3P)$
C	131.6	$S(3p^{-1}4d\,{}^3D^o) \rightarrow S({}^3P)$
C	132.3	$S(3p^{-1}4d\,{}^3D^o) \rightarrow S({}^3P)$
D	138.2	$S(3s^{-1}3p\,{}^3P^o) \rightarrow S({}^3P)$
D	138.5	$S(3s^{-1}3p\,{}^3P^o) \rightarrow S({}^3P)$
D	138.9	$S(3s^{-1}3p\,{}^3P^o) \rightarrow S({}^3P)$
D	139.3	$S(3s^{-1}3p\,{}^3P^o) \rightarrow S({}^3P)$
D	139.6	$S(3s^{-1}3p\,{}^3P^o) \rightarrow S({}^3P)$
D	140.2	$S(3p^{-1}5s\,{}^3S^o) \rightarrow S({}^3P)$
D	140.9	$S(3p^{-1}5s\,{}^3S^o) \rightarrow S({}^3P)$
E	142.5	$S(3p^{-1}3d\,{}^3D^o) \rightarrow S({}^3P)$
E	143.4	$S(3p^{-1}3d\,{}^3D^o) \rightarrow S({}^3P)$
E	143.8	$S(3p^{-1}3d\,{}^3D^o) \rightarrow S({}^3P)$
F	144.9	$S(3p^{-1}4s\,{}^1P^o) \rightarrow S({}^1D)$
$\underline{\text{G}}$	147.4	$S(3p^{-1}4s\,{}^3D^o) \rightarrow S({}^3P)$
$\underline{\text{H}}$	148.3	$S(3p^{-1}4s\,{}^3D^o) \rightarrow S({}^3P)$
$\underline{\text{H}}$	148.8	$S(3p^{-1}4s\,{}^3D^o) \rightarrow S({}^3P)$
$\underline{\text{I}}$	166.7	$S(3p^{-1}4s\,{}^1D^o) \rightarrow S({}^1D)$
$\underline{\text{J}}$	168.8	$S(3p^{-1}3d\,{}^1P^o) \rightarrow S({}^1S)$
K	178.2[b]	$S(3p^{-1}4s\,{}^1P^o) \rightarrow S({}^1S)$
$\underline{\text{L}}$	180.7[b]	$S(3p^{-1}4s\,{}^3S^o) \rightarrow S({}^3P)$
$\underline{\text{M}}$	182.0[b]	$S(3p^{-1}4s\,{}^3S^o) \rightarrow S({}^3P)$
$\underline{\text{M}}$	182.6[b]	$S(3p^{-1}4s\,{}^3S^o) \rightarrow S({}^3P)$

[a] The labels identify the peaks in Fig. 2, the excitation spectra in Fig. 3, the lines in Table I, and the dissociation processes in Table III.

[b] These lines are assigned following NIST Atomic Spectra Database [46] since they are out of the spectral range of Ref. [45].

TABLE III. Dissociation processes resulting in $H(2p)$ formation and S^* formation from H_2S and their dissociation limits calculated based on the energy levels of S atoms [46] and the dissociation energies of SH-H: 3.89 eV [47], S-H: 3.63 eV [47], and H-H: 4.4781 eV [48].

Label[a]	Fluorescence label[b]	Dissociation process	Dissociation limit (eV)
		Neutral dissociation	
1	G, H	$S(3p^{-1}4s\,{}^3D^o) + H_2(X\,{}^1\Sigma_g^+)$	11.45
2	I	$S(3p^{-1}4s\,{}^1D^o) + H_2(X\,{}^1\Sigma_g^+)$	11.62
3	J	$S(3p^{-1}3d\,{}^1P^o) + H_2(X\,{}^1\Sigma_g^+)$	13.14
4	L, M	$S(3p^{-1}4s\,{}^3S^o) + H_2(X\,{}^1\Sigma_g^+)$	9.90
5	L, M	$S(3p^{-1}4s\,{}^3S^o) + H(1s) + H(1s)$	14.38
6	A	$H(2p) + SH({}^2\Pi_i)$	14.09
7	A	$H(2p) + H(1s) + S({}^3P)$	17.72
8	A	$H(2p) + H(2p) + S({}^3P)$	27.92
		Dissociative ionization	
9	L, M	$S(3p^{-1}4s\,{}^3S^o) + H_2^+(X\,{}^2\Sigma_g^+) + e^-$	25.33
10	G, H	$S(3p^{-1}4s\,{}^3D^o) + H_2^+(X\,{}^2\Sigma_g^+) + e^-$	26.88
11	I	$S(3p^{-1}4s\,{}^1D^o) + H_2^+(X\,{}^2\Sigma_g^+) + e^-$	27.05
12	J	$S(3p^{-1}3d\,{}^1P^o) + H_2^+(X\,{}^2\Sigma_g^+) + e^-$	28.57
13	A	$H(2p) + SH^+(X\,{}^3\Sigma^-) + e^-$	24.52
14	A	$H(2p) + H(1s) + S^+({}^4S^o) + e^-$	28.08
15	A	$H(2p) + H^+ + S({}^3P) + e^-$	31.32

[a] The labels identify the dissociation limits in Figs. 3, 6, and 12.

[b] The same labels as in Tables I and II and Figs. 2 and 3.

of $B\eta^H_w$, we at last obtain the absolute values of $\sigma_{H(2p)}(E)$ in the photoexcitation of H_2S and H_2O.

III. RESULTS

A. Dispersed fluorescence experiments of H_2S

Figure 2 shows dispersed fluorescence spectra in the photoexcitation of H_2S at selected incident photon energies. The vertical axis shows the count rate normalized for the total gas pressure and incident photon flux and corrected for the sensitivity of the fluorescence spectrometer and detector used in the experiments. Each tick on the vertical axis shows a baseline of each spectrum. The vertical scales at energies of 14–24 eV are the same, whereas the vertical scales at energies of 25–35 eV are different from each other and also different from those at energies of 14–24 eV.

The Lyman-α fluorescence labeled A and fluorescences from excited S atoms (C–M) and S^+ ions (B) are observed, among which line A and the S^* lines G, H, I, J, L, and M are prominent. The observed lines are listed in Table II and are assigned as shown in the table following the results of the electron collision experiment on H_2S at 100 eV impact energy [45]. The alphabetical labels attached to the peaks in Fig. 2 are the same as those in Tables I–III and Fig. 3. The dissociation processes resulting in the formation of fragments that emit prominent lines in Fig. 2, i.e., lines A, G, H, I, J, L, and M, and their dissociation limits are summarized in Table III. The Lyman-α fluorescence, line A, is not observed at the incident photon energy of 14 eV, but is observed at energies higher than 15 eV, which is consistent with the fact that the lowest dissociation limit for the formation of $H(2p)$ atoms is 14.09 eV (label 6 in Table III). It turns out from Fig. 2 that the Lyman-α fluorescence is not dominant and the contribution of fluorescences from excited S atoms, i.e., lines G and H (147.4–148.8 nm), line I (166.7 nm), line J (168.8 nm), and lines L and M (180.7–182.6 nm), could not be ignored in the nondispersed fluorescence experiments as mentioned in Sec. II B 1. Figure 3 shows the excitation spectrum of the Lyman-α fluorescence as well as those of the prominent S^* fluorescences. The dissociation limits in Table III are shown in the relevant excitation spectra. It is remarkable that the excitation spectrum of lines L and M (182 nm), i.e., the $S(3p^{-1}4s\,{}^3S^o)$ fluorescence, rises at the second lowest dissociation limit of 14.38 eV (it rises at label

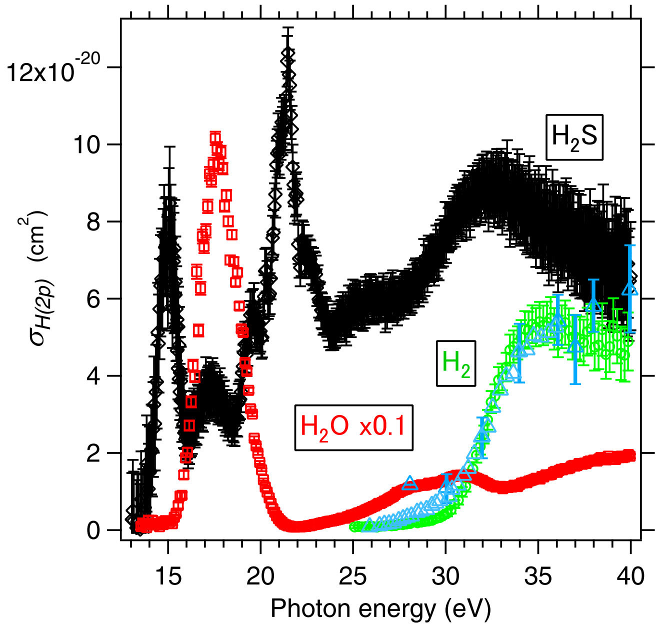

FIG. 4. The cross sections for the formation of H(2*p*) atoms in the photoexcitation of H_2S (open black diamonds), H_2O (open red squares), and H_2 (open green circles). The H_2 results are normalized to the cross section for H(2*p*) formation in the photoexcitation of H_2 on the absolute scale of the vertical axis (open blue triangles) [42].

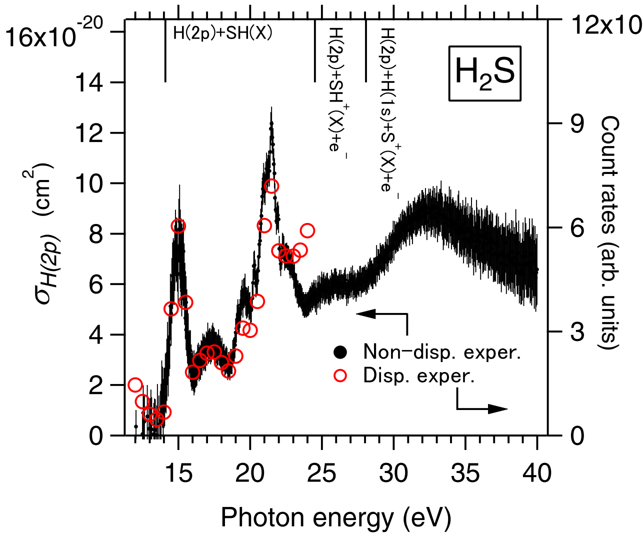

FIG. 5. The cross sections for the formation of H(2*p*) atoms $\sigma_{\mathrm{H}(2p)}(E)$ against the incident photon energy in the photoexcitation of H_2S obtained in the nondispersed fluorescence experiments (black closed circles with error bars, the left axis), which is the same as those in Fig. 4. The excitation spectrum for the Lyman-α fluorescence emission in Fig. 3 in the photoexcitation of H_2S obtained in the dispersed fluorescence experiments is also shown (open red circles, the right axis). The vertical bars show the dissociation limits of H(2*p*) formation processes indicated.

5 not label 4 in Table III), which shows that $\mathrm{S}(3p^{-1}4s\,^3S^o)$ atoms are produced through a three-body dissociation process, i.e., $\mathrm{S}(3p^{-1}4s\,^3S^o) + \mathrm{H}(1s) + \mathrm{H}(1s)$. The excitation spectra of other fluorescences rise at their lowest dissociation limits.

As mentioned just above, the superexcited H_2S molecules in the valence range produce a wide range of excited fragment atoms that emit vacuum ultraviolet fluorescence. On the other hand, the superexcited H_2O molecules in the valence range, as mentioned in Sec. II B 1, predominantly produce H(2*p*) fragment atoms and the branching ratio of the formation of O* fragment atoms, e.g., $\mathrm{O}^*(2p^{-1}3s\,^3S^o)$ atoms emitting the 130 nm fluorescence line, is much smaller than that of H(2*p*) atoms. The change of the major fragment atoms is discussed in Sec. IV C.

B. Nondispersed fluorescence experiments of H$_2$S and H$_2$O

In Fig. 4 are shown the cross sections for the formation of H(2*p*) atoms $\sigma_{\mathrm{H}(2p)}(E)$ in the photoexcitation of H_2S and H_2O as a function of the incident photon energy E, together with those in the photoexcitation of H_2 as the reference result. These cross sections have been obtained following the procedure mentioned in Sec. II B 2. The values of $\sigma^{\mathrm{H}_2}_{\mathrm{H}(2p)}(E)$ reported by [42] are also shown (open blue triangles), to which cross sections the relative values of $\sigma^{\mathrm{H}_2}_{\mathrm{H}(2p)}(E)$ in the present experiment (open green circles) are normalized at the threshold range so that the value of $B\eta^H_w$ in Eq. (10) for H_2S and Eq. (11) for H_2O is obtained as mentioned in Sec. II B 2. The error bars express the statistical uncertainties of the count rates $\dot{N}_w(E)$ and $\dot{N}_{\mathrm{wo}}(E)$ in Sec. II B 1, and the law of propagation of errors is considered.

We compare the $\sigma^{\mathrm{H_2S}}_{\mathrm{H}(2p)}(E)$ curve in Fig. 4 with the excitation spectrum for the emission of the Lyman-α fluorescence obtained in the dispersed fluorescence experiments of H_2S (the top panel of Fig. 3) in terms of shape in order to substantiate the procedure of separating the Lyman-α fluorescence in the nondispersed experiments of H_2S mentioned in Sec. II B 1. The result of the comparison is shown in Fig. 5. The agreement between the $\sigma^{\mathrm{H_2S}}_{\mathrm{H}(2p)}(E)$ curve and the excitation spectrum in terms of shape justifies our procedure of separating the Lyman-α fluorescence from other fluorescences in the nondispersed experiments of H_2S. The small disagreement in the lower energy range seems probably due to the noise of the detector in the dispersed fluorescence experiments and that around 24 eV seems probably due to the small intensity of the incident light beam in the dispersed fluorescence experiments.

The relative values of the sum of the sensitivity-weighted cross sections for the emission of S* (S^{+*}) fluorescences $\sum_\beta \eta^\beta_w \langle q_\beta \rangle(E)$ are obtained in the photoexcitation of H_2S following Eq. (9) in addition to the $\sigma^{\mathrm{H_2S}}_{\mathrm{H}(2p)}(E)$ and are shown against the incident photon energy in Fig. 6, where β runs in the range 121.6–200 nm (121.6 nm is not included). We note that $\langle q_\beta \rangle(E)$ is approximated by $\sigma_\beta(E)/(4\pi)$, where $\sigma_\beta(E)$ is the angle-integrated cross section for the emission of the fluorescence β, because of the magic angle. The sum of the excitation spectrum for the S* lines G and H and that for the S* line I multiplied by 0.1 (see Fig. 3) is also shown in Fig. 6 and the shape is reasonably in good agreement with that of $\sum_\beta \eta^\beta_w \sigma_\beta(E)$. The contribution of S^{+*} lines seems to be negligibly small at least in the range below 24 eV in the $\sum_\beta \eta^\beta_w \sigma_\beta(E)$ curve. The factor 0.1 suggests that the detection

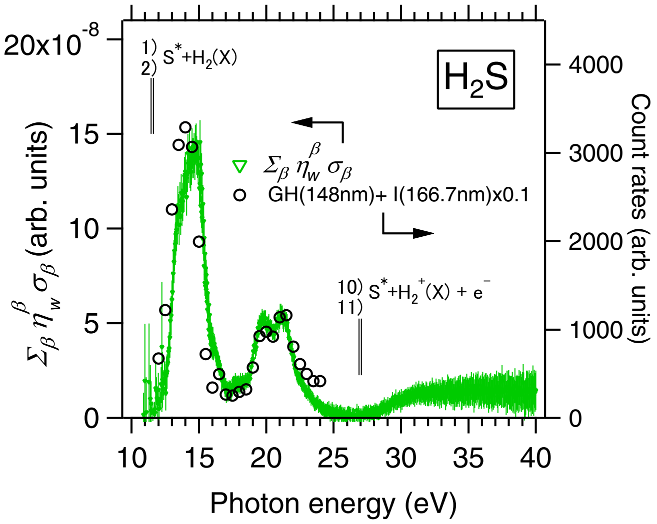

FIG. 6. The sum of the sensitivity-weighted cross sections for the emission of S* (S^{+*}) fluorescences, $\sum_\beta \eta_w^\beta \sigma_\beta(E)$, on a relative scale against the incident photon energy in the photoexcitation of H_2S (open green triangles, the left axis). The sum of the excitation spectrum for the S* lines G and H and that for the S* line I multiplied by 0.1 is also shown (open black circles, the right axis). The vertical bars show the dissociation limits listed in Table III (the numerical labels are the same).

efficiency of the present MCP with CsI coating decreases more noticeably with increasing wavelength than the literature one in Table I [44].

IV. DISCUSSION

The ground electronic states of H_2O and H_2S in C_{2v} symmetry are [49]

H_2O $\tilde{X}\,{}^1A_1$:

$$\underbrace{(\mathrm{O}1s)^2}_{\substack{\text{inner shell}\\ \text{orbital}}}\ \underbrace{(2a_1)^2}_{\substack{\text{inner valence}\\ \text{orbital}}}\ \underbrace{(1b_2)^2(3a_1)^2(1b_1)^2}_{\text{outer valence orbitals,}}$$

H_2S $\tilde{X}\,{}^1A_1$:

$$\underbrace{(\mathrm{S}1s)^2(\mathrm{S}2s)^2(\mathrm{S}2p)^6}_{\substack{\text{inner shell}\\ \text{orbitals}}}\ \underbrace{(4a_1)^2}_{\substack{\text{inner valence}\\ \text{orbital}}}\ \underbrace{(2b_2)^2(5a_1)^2(2b_1)^2}_{\text{outer valence orbitals}}.$$

From now on, the parentheses attached to orbitals are omitted unless it is misleading. The correlation of valence orbitals between H_2O and H_2S is obvious. The bond length and bond angle of H_2O in the ground electronic state are 0.956 Å and 105.2°, respectively, and those of H_2S in the ground electronic state are 1.328 Å and 92.2°, respectively [49]. The inner valence orbital in H_2O/H_2S is from the O $2s$/ S $3s$ orbital and H $1s$ orbital, respectively, and outer valence orbitals in H_2O/H_2S are mainly from the O $2p$/ S $3p$ orbital and H $1s$ orbital, respectively [32]. The vertical ionization potentials of H_2O for the $1b_1^{-1}$, $3a_1^{-1}$, $1b_2^{-1}$, and $2a_1^{-1}$ states are 12.6, 14.8, 18.6, and 32.6 eV, respectively [35]. Those of H_2S for the $2b_1^{-1}$, $5a_1^{-1}$, $2b_2^{-1}$, and $4a_1^{-1}$ states are 10.46, 13.45, 15.55, and 22.08 eV, respectively [36]. The ionization potentials of H_2S are lower than those of H_2O as seen in Fig. 1. The electronic structures of H_2O and H_2S are similar to each other since both molecules have the same symmetry properties and have eight valence electrons as above. However, the electronic structure of H_2S is contracted in comparison with that of H_2O in terms of energy as mentioned in Sec. I. The similarity and difference between the electronic structures of H_2O and H_2S are illustrated in Fig. 1. It is again stressed that the energy gap between the $2b_2^{-1}$ state (the highest outer valence ionized state) and the $4a_1^{-1}$ state (the inner valence ionized state) of H_2S^+, 6.5 eV, is much narrower than the energy gap between the corresponding $1b_2^{-1}$ state and the $2a_1^{-1}$ state of H_2O^+, 14.0 eV. The electron correlation for the superexcited states of H_2S in the inner valence range is expected to become stronger than the electron correlation for those of H_2O in the inner valence range because of the denser population of the superexcited states of H_2S than those of H_2O. This is supported by the experimental photoelectron spectra of H_2O [35] and H_2S [36,57] in the inner valence range shown in Figs. 9(b) and 9(d), respectively, and the monopole intensities calculated with the SAC-CI general-R method [53] [the vertical bars in Figs. 9(b) and 9(d)]. Figures 9(b) and 9(d) are described in detail in the following subsections. It is obvious that the experimental photoelectron spectra of H_2O and H_2S in the inner valence range are accounted for by the monopole intensities considering the fixed nuclei approximation used in the calculation and the estimated energy resolution in the experimental photoelectron spectra, 1 eV for H_2O and a few hundred meV for H_2S. The more double-hole one-electron states (green bars) appear around the "$4a_1^{-1}$" states (red bars) in H_2S than around the "$2a_1^{-1}$" states (red bars) in H_2O and the intensity difference between the red and green bars in H_2S is not as large as in H_2O. The "$4a_1^{-1}$" and "$2a_1^{-1}$" states are single-hole states to the zeroth order approximation and in fact multiconfiguration states as mentioned in detail in Secs. IV A and IV B. It turns out that the electron correlation in the electronic states of H_2S^+ in the inner valence range is stronger than in those of H_2O^+, which conclusion supports the expectation mentioned above. We hence discuss the effect of the increasing electron correlation on molecular superexcited states from the comparison of the H_2S results with those of H_2O. The dipole oscillator strength is a key quantity in the comparison.

The absolute cross sections for the formation of H($2p$) atoms, $\sigma_{\mathrm{H}(2p)}(E)$, in the photoexcitation of H_2O and H_2S are shown in Fig. 4. The cross section of the channel j in the photoexcitation by a photon of energy E, $\sigma_j(E)$, is related to the density of the dipole oscillator strength (DOS) of the channel j per unit range of energy E, df_j/dE, by

$$\sigma_j(E) = 4\pi^2\alpha a_0^2 \frac{df_j}{d(E/R)}, \tag{12}$$

where α is the fine structure constant, R is the Rydberg energy, and a_0 is the Bohr radius [50]. Equation (12) is more conveniently written as

$$\sigma_j(E) = 1.098 \times 10^{-16}\left(\frac{df_j}{dE}\right), \tag{13}$$

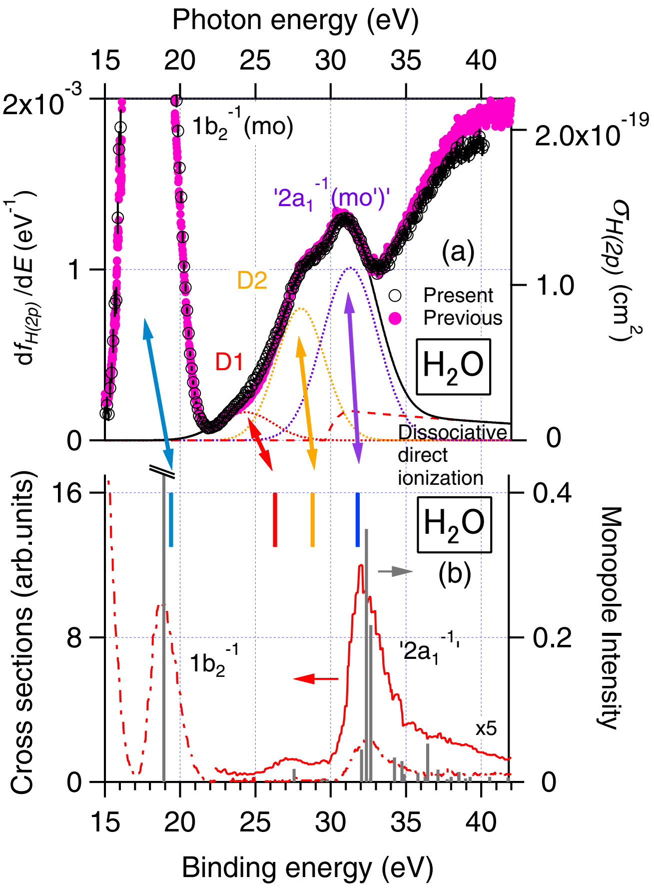

FIG. 7. (a) Densities of the dipole oscillator strength for the formation of $\mathrm{H}(2p)$ atoms in $\mathrm{H_2O}$ as a function of incident photon energy. Open circles: Present results on an absolute scale of the vertical axis. Closed red circles: Relative results measured by Nakano *et al.* [20] normalized around 30 eV to the absolute ones by the present study. The right vertical axis shows the absolute scale of the cross sections for the formation of $\mathrm{H}(2p)$ atoms according to Eq. (12). The curves show the best result of the peak separation by Nakano *et al.* [20] (see Sec. IV A). The superexcited states involved, i.e., the singly excited $1b_2^{-1}(\mathrm{mo})$ state and doubly excited $D1$, $D2$, and "$2a_1^{-1}(\mathrm{mo}')$" states, are seen and summarized in Table IV. (b) The photoelectron spectrum of $\mathrm{H_2O}$ recorded at a photon energy of 60 eV and quasimagic angle with an estimated energy resolution of 1 eV (solid and dashed curves) [35] together with the corresponding spectrum, i.e., the monopole intensity for each state of $\mathrm{H_2O^+}$ calculated using the SAC-CI general-R method (vertical bars) [53]. The monopole intensities were calculated in the range up to 41.78 eV. The energies of the ion cores on which the superexcited states in (a) are built are also shown (vertical bars with arrows) [20].

where $\sigma_j(E)$ is expressed in cm^2 and df_j/dE in eV^{-1}. The integration of df_j/dE originating from the electronic state s over the range of E gives the DOS for the channel j from the state s, which is denoted by f_j^s.

In the following subsections we discuss the superexcited states involved in the cross sections for the formation of $\mathrm{H}(2p)$ atoms in the photoexcitation of $\mathrm{H_2O}$ and $\mathrm{H_2S}$ in Fig. 4 and then the DOSs for the formation of $\mathrm{H}(2p)$ atoms originating from those superexcited states, i.e., state-resolved DOSs.

A. Doubly excited states of $\mathrm{H_2O}$ resulting in $\mathrm{H}(2p)$ formation

The present cross section curve for $\mathrm{H}(2p)$ formation from $\mathrm{H_2O}$ on the absolute scale is compared with the previous one on the relative scale [20] (emission along the unit polarization vector of the linearly polarized incident light) in terms of shape in Fig. 7(a), where both are normalized around 30 eV. Their shapes agree well with each other. The precursor superexcited states found in Ref. [20] are hence supported by the present investigation, and the absolute values of the state-resolved DOSs for $\mathrm{H}(2p)$ formation are determined as shown below.

According to [20], the peak around 17.5 eV in Fig. 7(a), which is out of scale of the vertical axis, was assigned the singly excited $1b_2^{-1}(\mathrm{mo})$ state, where the symbol "mo" stands for a molecular orbital. The assignment of the band in the higher energy range is not so simple. In Ref. [20], the band was separated to the peaks due to precursor superexcited states with the fitting based on the multidimensional reflection approximation [51] and the semiclassical treatment of the decay dynamics of the superexcited molecules involved [52]: the DOS density for the $\mathrm{H}(2p)$ formation originating from the dissociative electronic state s, $df^s_{\mathrm{H}(2p)}/dE$, is given by

$$df^s_{\mathrm{H}(2p)}/dE = A_s E \exp\left[-\left(\frac{E-E_s}{B_s}\right)^2\right], \tag{14}$$

where A_s, B_s, and E_s are constants independent of E. In Fig. 7(a), the best result of the fitting is also shown [dotted curves: peaks due to superexcited states at $E_s = 24.2$, 27.9, and 31.2 eV, dashed curve: a component of the dissociative direct ionization of $\mathrm{H}(2p) + \mathrm{OH}^+(X) + e^-$, solid curve: the sum of them]. We do not need to separate the peaks in the present DOS density curve in Fig. 7(a) since it is in good agreement with the curve of [20]. The states of $\mathrm{H_2O^+}$ are shown in Fig. 7(b) because each precursor superexcited state of $\mathrm{H}(2p)$ atoms in Fig. 7(a) is built on any of those ionic states such that one electron is bound on an ion. Figure 7(b) shows the photoelectron spectrum of $\mathrm{H_2O}$ taken at a photon energy of 60 eV and quasimagic angle with an estimated energy resolution of 1 eV [35] together with the monopole intensity for each ionic state calculated using the SAC-CI general-R method [53]. The superexcited states of $\mathrm{H_2O}$ lie in energy slightly below their ion-core states. To visualize this stability, the density of the dipole oscillator strength for the photoabsorption of $\mathrm{H_2O}$ is shown in the range just below the ionization threshold of the outermost $1b_1$ electron [33] (see Fig. 8), where the energy is in reference to the ionization threshold of the $1b_1$ electron, 12.6 eV [35]. The peaks below the ionization threshold except for that around -3 eV are attributed to the neutral states built on the $1b_1^{-1}$ state of $\mathrm{H_2O^+}$ ions. Figure 8 shows that neutral states of $\mathrm{H_2O}$ are stabilized with the binding of one electron by an $\mathrm{H_2O^+}$ ion by at most several eV.

The superexcited states of $\mathrm{H_2O}$ resulting in $\mathrm{H}(2p)$ formation are summarized in Table IV together with the ion-core states on which those superexcited states are built. (i) The superexcited state at 17.5 eV is a singly excited $1b_2^{-1}(\mathrm{mo})$ state built on the single-hole $1b_2^{-1}$ ion-core state. The $1b_2^{-1}(\mathrm{mo})$ state is a single-configuration state and is described within

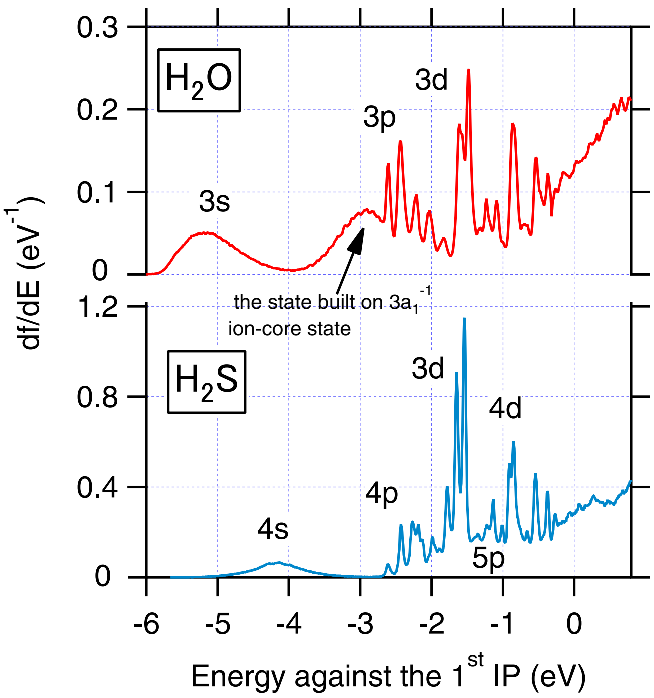

FIG. 8. Densities of the dipole oscillator strengths for the photoabsorption of H_2O [33] and H_2S [34] as a function of incident photon energy measured with a resolution of 50 meV. Only the parts below their first ionization potentials, i.e., the parts below the $1b_1^{-1}$ state of H_2O^+ and $2b_1^{-1}$ state of H_2S^+, are shown. The energy on the horizontal axis is the one with respect to the first ionization potential. The assignments of the peaks for H_2O and H_2S follow Refs. [33,54], respectively. This figure shows an example on how neutral states are stabilized with the binding of one electron by an ion.

the independent electron model. (ii) The superexcited states at 24.2 and 27.9 eV are the doubly excited $D1$ and $D2$ states. The energies of the ion cores of the $D1$ and $D2$ states are indicated in Fig. 7(b). The doubly excited $D1$ and $D2$ states are multiconfiguration states expressed as superpositions of doubly excited configurations with negligible contributions of the singly excited configurations. (iii) The superexcited state at 31.2 eV is a "$2a_1^{-1}$(mo′)" state built on a "$2a_1^{-1}$" ion-core state. The quotation marks indicate a strong configuration mixing due to electron correlations. The "$2a_1^{-1}$" ion-core state itself is described with a superposition of the single-hole $2a_1^{-1}$ configuration and double-hole one-electron configurations, in which superposition the contribution of the former is no longer dominant [53] as shown in Table IV. The "$2a_1^{-1}$(mo′)" state is hence described with a superposition of the singly excited $2a_1^{-1}$(mo′) configuration and doubly excited configurations. The contribution of the former seems not to be dominant as in the "$2a_1^{-1}$" ion-core state. The "$2a_1^{-1}$(mo′)" state is hence classified as a doubly excited state. The doubly excited $D1$, $D2$, and "$2a_1^{-1}$(mo′)" states are not so amenable to the independent electron model that they are described with superpositions of multiple configurations, whereas the singly excited $1b_2^{-1}$(mo) state is amenable to the independent electron model and it is thus described with just a single configuration.

Taking advantage of the absolute cross sections in Fig. 7(a), the DOS for H(2p) formation due to each superexcited state s in Fig. 7(a), $f^s_{H(2p)}$, is obtained following

$$f^s_{\mathrm{H}(2p)} = \int \left(df^s_{\mathrm{H}(2p)}dE\right)dE, \tag{15}$$

where $s = 1b_2^{-1}$(mo), $D1$, $D2$, and "$2a_1^{-1}$(mo′)" states. The values of $f^s_{\mathrm{H}(2p)}$ are summarized in Table IV and shown diagrammatically in Fig. 9(a), where the position of the vertical bar is equal to E_s in Eq. (14) and the length is equal to $f^s_{\mathrm{H}(2p)}$. Figure 9(a) is referred to as the DOS pattern. In Fig. 9(b), the experimental photoelectron spectrum and calculated monopole intensities in Fig. 7(b) are displayed again to show the ionic states on which the precursor superexcited states of H(2p) atoms are built.

It is interesting that the band in the Balmer-α cross section curve around the O 1s shake-up limit [55] has a shape similar to the inner valence band in the cross section curve in Fig. 7(a) (see Fig. 10). This indicates that similar excited orbitals are involved in the doubly excited states built on the ion-core states in the inner valence range and O 1s^{-1} shake-up states.

TABLE IV. The superexcited states of H_2O resulting in H(2p) formation.

Superexcited states				Ion-core states of the superexcited states to the left			
State index s	Energy (eV)[c]	Electronic state	DOS[a] ($\times10^{-3}$)	Energy (eV)[d]	Energy (eV)[b]	Monopole intensity[b]	Main configurations[b] ($C > 0.3$)
1	17.5	$1b_2^{-1}$(mo)	23.8	19.4	18.92	0.893	$(1b_2^{-1})$
2	24.2	$D1$	0.77	26.3	27.56	0.018	$0.54(1b_1^{-2}12a_1) - 0.45(1b_1^{-2}16a_1) + 0.38(1b_1^{-2}8a_1)$
3	27.9	$D2$	3.15	28.8			
4	31.2	"$2a_1^{-1}$(mo′)"	4.68	31.8	32.37	0.350	$0.59(2a_1^{-1}) - 0.31(3a_1^{-2}12a_1)$
					32.66	0.217	$0.46(2a_1^{-1})$

[a] State-resolved dipole oscillator strengths for the formation of H(2p) atoms in the photoexcitation of H_2O (present results).
[b] Calculated results with the SAC-CI general-R method [53].
[c] Experimental values of E_s in Eq. (14) [20].
[d] Experimental values obtained with the Rydberg-like formula [20].

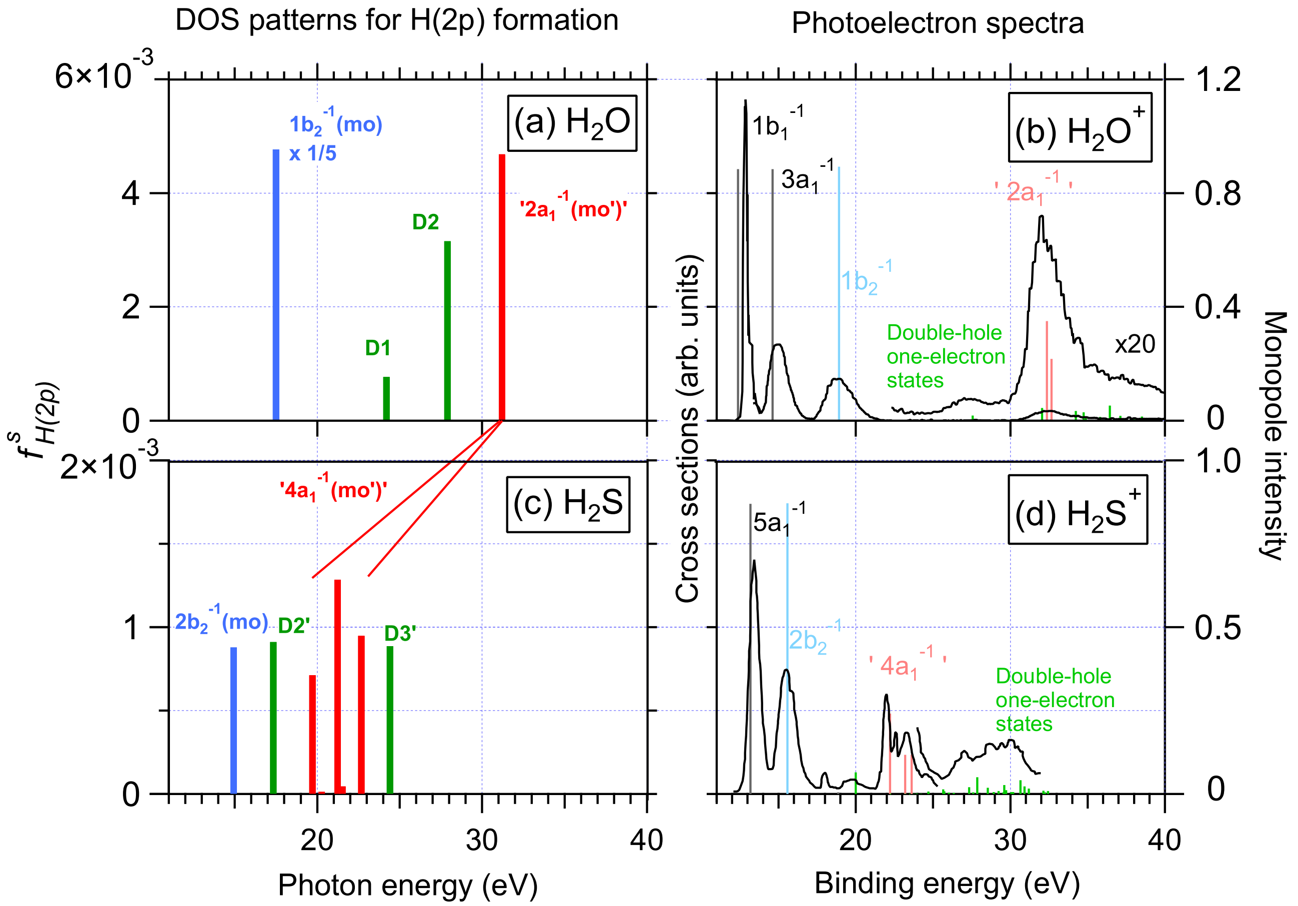

FIG. 9. The state-resolved dipole oscillator strengths (DOSs) for H($2p$) formation in the photoexcitation of H_2O in (a) and H_2S in (c) obtained in the present experiments (thick vertical bars) together with the experimental and theoretical photoelectron spectra of H_2O in (b) and H_2S in (d), which are the same as Figs. 7(b) and 11(b), respectively, but the ranges of the binding energy here are wider than in Figs. 7(b) and 11(b). The monopole intensities, the vertical bars in (b) and (d), were calculated in the range up to 41.78 eV for H_2O and in the range up to 32.44 eV for H_2S [53].

B. Doubly excited states of H_2S resulting in H($2p$) formation

In this section we investigate the superexcited states of H_2S involved in the cross section curve for H($2p$) formation in Fig. 4 following the same way as in H_2O. The contribution of each superexcited state, Eq. (14), is separated from the cross section curve through fitting. There is a possibility that dissociative ionizations contribute in the range above 24.5 eV according to the dissociation limits in Table III. Below 28.1 eV, the ionic partner of H($2p$) atoms is limited to $SH^+(X)$ ions. We approximate the cross section of the dissociative direct ionization of H($2p$) + $SH^+(X) + e^-$ in the photoionization of H_2S by $a'\sigma_{SH^+}(E - b')$, where $\sigma_{SH^+}(E)$ is the cross section of the dissociative direct ionization of H($1s$) + $SH^+(X)$ + e^- in the photoionization of H_2S, and a factor a' and amount of shift b' are constants independent of E. The value of b' would be close to the energy difference between the $2p$ and $1s$ levels of a hydrogen atom. We use the cross section of the formation of SH^+ in the photoionization of H_2S measured by Feng *et al.* [56] as $\sigma_{SH^+}(E)$, since their cross sections seem to be dominated by the dissociative direct ionization of H($1s$) + $SH^+(X) + e^-$. We hence fit the following equation to the DOS density curve for H($2p$) formation from H_2S in Fig. 11(a) in the range 12.7–28.1 eV,

$$df_{H(2p)}dE = \sum_s A'_s E \exp\left[-\left(\frac{E - E'_s}{B'_s}\right)^2\right] + a'\sigma_{SH^+}(E - b'), \qquad (16)$$

where A'_s, B'_s, E'_s, a', and b' are fitting parameters. The resolution of the incident photon energy, i.e., 50 meV at 21 eV incident photon energy, is not taken into account since each component in Fig. 11(a) seems much wider than the resolution except for two sharp peaks around 20 and 22 eV. The prime is attached to each fitting parameter to distinguish it from the corresponding parameter in H_2O.

A good fit has been obtained with eight superexcited states (s = 1–8) as shown in Fig. 11(a) [dotted curve: peak originating from superexcited state s in Eq. (16), dashed curve: a component of the dissociative direct ionization of H($2p$) + $SH^+(X) + e^-$ in Eq. (16), solid curve: the sum of them]. The energies E'_s and widths B'_s of the eight superexcited states are summarized in Table V. Those superexcited states have been found by extracting the discrete state from the superposition with the ionization continuum through the detection of

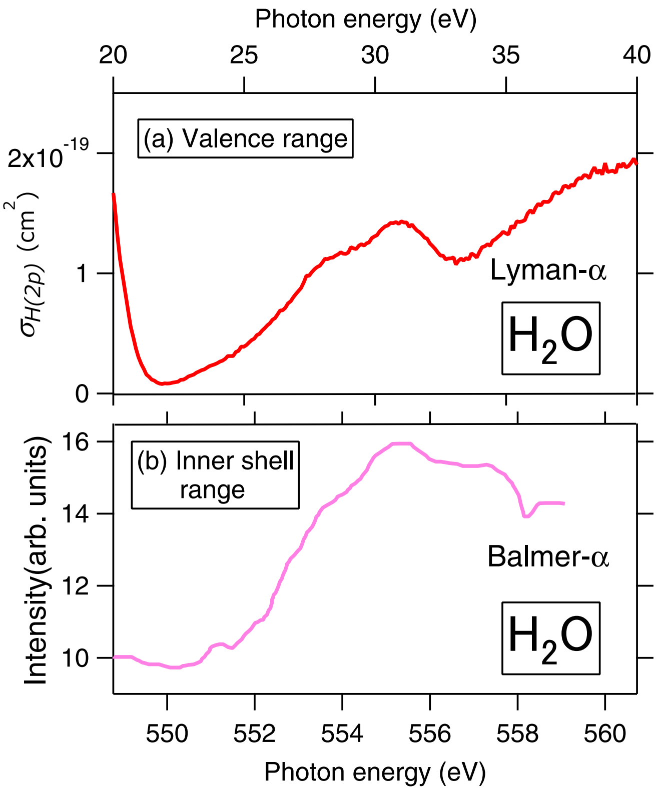

FIG. 10. (a) Cross sections for H($2p$) formation in the photoexcitation of H_2O in the inner valence range recorded with an energy resolution of 100 meV at 30 eV photon energy, which is the same as the present result in Fig. 7(a). (b) Cross sections for the emission of the Balmer-α fluorescence in the photoexcitation of H_2O in the O $1s$ inner shell range recorded with an energy resolution of 120 meV (Fig. 2 in Ref. [55]). The zero level of the cross sections is not clear in Ref. [55]. The energy scale in (b) is enlarged in comparison with that in (a).

the Lyman-α fluorescence. The shapes of the narrow peaks labeled 4 and 6 may be influenced by the energy resolution (50 meV at 21 eV incident photon energy).

The superexcited states in Fig. 11(a) are likely to contribute to the formation of S* atoms through neutral dissociation. We hence fit Eq. (16) again to the $\sum_\beta \eta_w^\beta \sigma_\beta(E)$ curve in Fig. 6 (open green triangles), which is the sum of the sensitivity-weighted cross section curves for the S* fluorescences. In the fitting, A'_s ($s = 1$–8) is a fitting parameter, but B'_s and E'_s ($s =$ 1–8) are taken to be the same as those obtained in the fitting to the cross section curve for H($2p$) formation in Fig. 11(a) since B'_s and E'_s are inherent in the superexcited state s. The contribution of the dissociative ionization is negligible in the $\sum_\beta \eta_w^\beta \sigma_\beta(E)$ curve in the range below 27 eV as seen in Fig. 6, and hence only the first term on the right-hand side of Eq. (16) is fitted in the range below 27 eV. In fact, two superexcited states in the range 13–17 eV ($s = \bar{1}, \bar{2}$) are appended in order to obtain a good fit as seen in Fig. 12 [dotted curve: peak originating from superexcited state s in Eq. (16), solid curve: the sum of them]. In the fitting A'_s, B'_s, and E'_s ($s = \bar{1}, \bar{2}$) are fitting parameters appended to a set of fitting parameters A'_s ($s = 1$–8). The energies E'_s and widths B'_s for the superexcited states $s = \bar{1}$ and $\bar{2}$ are also shown in Table V.

Let us substantiate the superexcited states of H_2S found in Figs. 11(a) and 12, following the same line as for H_2O: the superexcited states of H_2S are considered neutral states built on ion-core states such that one electron is bound on an H_2S^+ ion. It is hence significant to summarize the electronic states of H_2S^+, which were extensively studied by the photoelectron spectroscopy in the valence range [36,57,58]. The photoelectron spectrum of H_2S taken at a photon energy of 90 eV with the estimated energy resolution of a few hundred meV (solid curve) [57] and that taken at a photon energy of 1487 eV with the similar energy resolution to that in Ref. [57] (dashed curve) [36] are shown in Fig. 11(b) together with the corresponding spectrum (vertical bars), i.e., the monopole intensity for each ionic state calculated using the SAC-CI general-R method [53]. The states of H_2S^+ that appear with considerable intensities in the experimental and theoretical photoelectron spectra are listed in Table V. The peak at 15.6 eV in the experimental photoelectron spectrum in Fig. 11(b) is attributed to the single-hole $2b_2^{-1}$ state with negligible contributions from other configurations. The small feature around 18 eV is due to an OCS impurity [57]. The assignment of the peaks in the inner valence range is not so simple as that in the outer valence range. Baltzer *et al.* [57] observed a complicated feature in the range 19–25 eV in the experimental photoelectron spectrum in Fig. 11(b) and attributed them to four states labeled state 1 to state 4. It is seen from the spectrum [57] measured with the much higher energy resolution than in Fig. 11(b) that the manifold of state 3 comprises four vibrational peaks, among which two peaks are noticeable, and the manifold of state 4 comprises seven vibrational peaks, which are not well separated. The SAC-CI general-R calculation explains the state 1 to state 4 as seen in Fig. 11(b). We note that the fixed nuclei approximation was used in the SAC-CI general-R calculation [53]. As shown in Table V the state 1 is expressed as the superposition of the double-hole one-electron configurations with a negligible contribution of single-hole configurations. Each of the states 2 to 4 is expressed as a superposition of the single-hole $4a_1^{-1}$ configuration and double-hole one-electron configurations, where the contributions of the double-hole one-electron configurations are comparable to or even larger than that of the single-hole $4a_1^{-1}$ configuration [53] as seen in Table V. States 2–4 are multiconfiguration states, and they are thus referred to as the "$4a_1^{-1}$" states. The quotation marks show that they are in fact multiconfiguration states due to the electron correlation as for H_2O. The manifold of states 1–4 is followed by the weaker and broad structure in the range above 26 eV [36,58] as seen in Fig. 11(b). This structure is attributed to the states of H_2S^+ expressed as superpositions of double-hole one-electron configurations as seen in Table V based on the SAC-CI general-R calculation [53].

We then substantiate the superexcited states of H_2S in Table V following the line that they are built on any of the states of H_2S^+ ions in Fig. 11(b). The superexcited states of H_2S lie in energy slightly below their ion-core states. To visualize this stability, the density of the dipole oscillator strength for the photoabsorption of H_2S is shown in the range just below the ionization threshold of the outermost $2b_1$ electron [34] (see Fig. 8), where the energy is in reference to

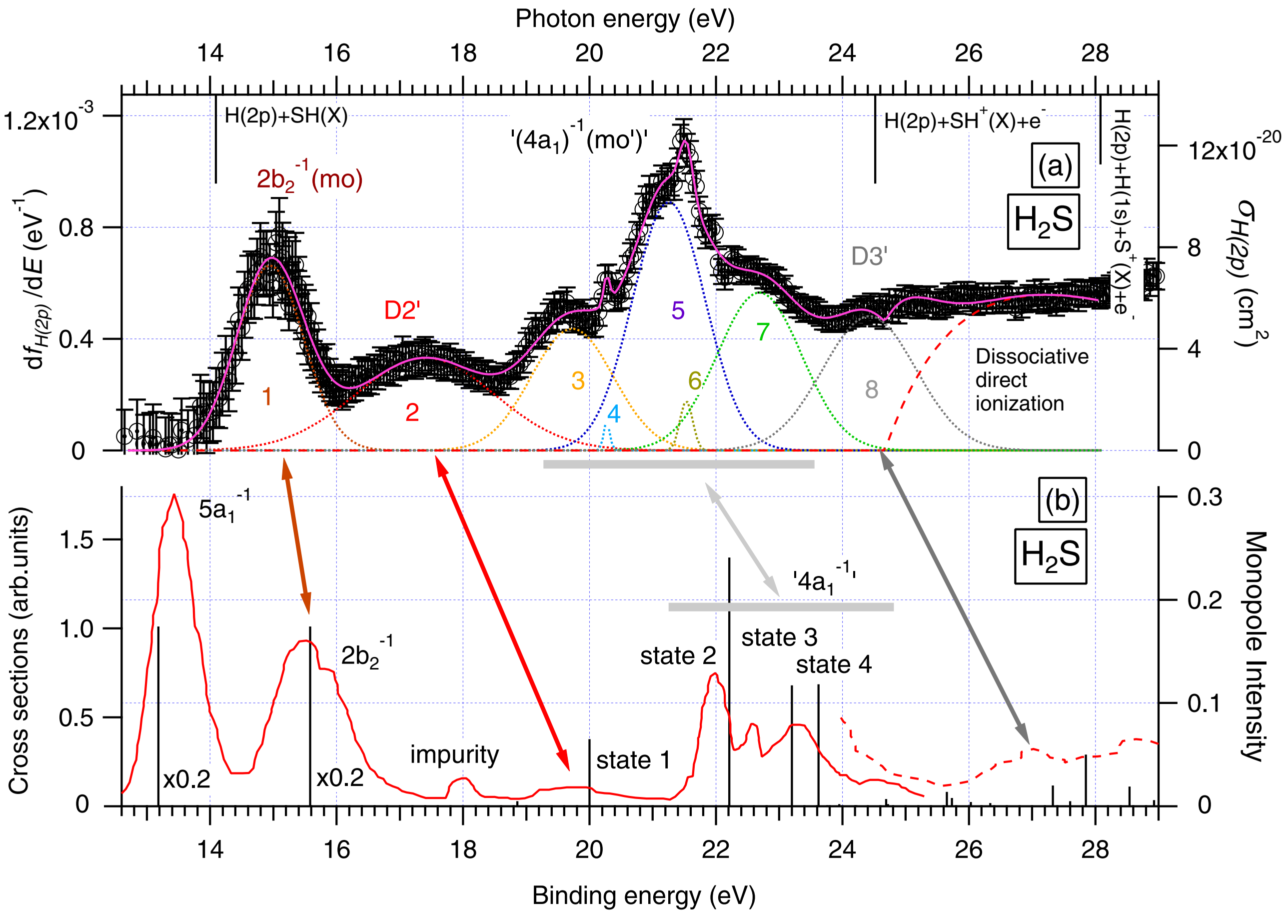

FIG. 11. (a) Densities of the dipole oscillator strength for the formation of H(2*p*) atoms in H_2S as a function of incident photon energy. The curves show the best result of the fitting of Eq. (16) [dotted curve: peak originating from superexcited state *s* in Eq. (16), dashed curve: a component of the dissociative direct ionization of H(2*p*) + $SH^+(X) + e^-$ in Eq. (16), solid curve: the sum of them]. The superexcited states involved are summarized in Table V. (b) The photoelectron spectra of H_2S are displayed to show the states of H_2S^+ ions on which the superexcited states of H_2S in (a) are built. The arrows connect the superexcited states and their ion-core states. The photoelectron spectra were measured at a photon energy of 90 eV and with an estimated energy resolution of a few hundred meV (solid curve) [57] and at 1487 eV photon energy and with the similar energy resolution (dashed curve) [36]. Vertical bars show monopole intensities for states of H_2S^+ ions calculated using the SAC-CI general-*R* method [53] (see Table V). They were calculated in the range up to 32.44 eV.

the ionization threshold of the $2b_1$ electron, 10.46 eV [36]. The peaks below the ionization threshold are attributed to the neutral states built on the $2b_1^{-1}$ state of H_2S^+ ions. Figure 8 shows that neutral states of H_2S are stabilized with the binding of one electron by an H_2S^+ ion by at most several eV.

The superexcited states at 13.7 eV ($s = \bar{1}$) and 14.9 eV ($s = 1$) are built on the $2b_2^{-1}$ ion-core state, and thus they are referred to as the $2b_2^{-1}$(mo) states. The $2b_2^{-1}$(mo) states of H_2S are single-configuration states such as the $2b_2^{-1}$ ion-core state of H_2S^+. However, other superexcited states ($s = \bar{2}$ and 2–8) are multiconfiguration states as discussed below.

The superexcited states at 16.2 eV ($s = \bar{2}$) and 17.3 eV ($s = 2$) seem to be built on the ion-core state at 19.6 eV found by Baltzer *et al.* [57] [state 1 in Fig. 11(b)]. This ion-core state is described as the superposition of the double-hole one-electron configurations [53] as seen in Table V. It is concluded that the superexcited states at 16.2 eV ($s = \bar{2}$) and 17.3 eV ($s = 2$) are doubly excited states, and are multiconfiguration states with a negligible contribution of singly excited configurations such as their ion-core states. The doubly excited states at 16.2 and 17.3 eV are referred to as the $D1'$ and $D2'$ states, respectively, where the prime is attached to distinguish them from the doubly excited $D1$ and $D2$ states of H_2O.

The superexcited states in the range 19.7–22.7 eV ($s =$ 3–7) seem to be built on the states 2–4 of H_2S^+ ions, i.e., they seem to be built on the "$4a_1^{-1}$" ion-core states. Those ion-core states are expressed as superpositions of the single-hole $4a_1^{-1}$ configuration and double-hole one-electron configurations, in which superpositions the contributions of the double-hole one-electron configurations are comparable to or even larger than that of the single-hole $4a_1^{-1}$ configuration [53] as seen in Table V. It is concluded that the superexcited states in the range 19.7–22.7 eV ($s =$ 3–7) are multiconfiguration states, and the contributions of the doubly excited configurations are comparable to or even larger than that of the singly excited $4a_1^{-1}$(mo′) configuration as in the "$4a_1^{-1}$" ion-core states. The superexcited states in the range 19.7–22.7 eV ($s =$ 3–7) are referred to as the "$4a_1^{-1}$(mo′)" states and are classified as

TABLE V. The superexcited states of H_2S resulting in H($2p$) and S* formation. The states with $s = 1$–8 contribute to both H($2p$) and S* formation, but those with $s = \bar{1}$ and $\bar{2}$ contribute to only S* formation. In the main configurations, the $4a_1^{-1}$ is underlined.

Superexcited states					Ion-core states of the superexcited states to the left			
State index s	Energy E_s' (eV)	Width B_s' (eV)	Electronic state	DOS[a] ($\times 10^{-3}$)	Energy (eV)	Energy (eV)[d]	Monopole intensity[d]	Main configurations[d] ($C > 0.3$)
$\bar{1}$	13.7	0.95	$2b_2^{-1}$(mo)		15.55[b]	15.58	0.871	$(2b_2^{-1})$
1	14.9	0.75	$2b_2^{-1}$(mo)	0.88				
$\bar{2}$	16.2	0.48	$D1'$		19.6 (state 1)[c]	20.00	0.065	$0.57(2b_1^{-2}15a_1) - 0.43(2b_1^{-2}11a_1)$
2	17.3	1.6	$D2'$	0.91				
3	19.7	0.92	“$4a_1^{-1}$(mo′)”	0.71	22.08 (state 2)[c]	22.21	0.241	$0.49(\underline{4a_1^{-1}}) - 0.35(2b_1^{-2}16a_1) + 0.34(2b_1^{-2}11a_1) - 0.33(2b_1^{-2}7a_1)$
4	20.3	0.07	“$4a_1^{-1}$(mo′)”	0.01				
5	21.2	0.82	“$4a_1^{-1}$(mo′)”	1.28	22.67, 22.95 (state 3)[c]	23.20	0.117	$0.36(\underline{4a_1^{-1}}) + 0.44(2b_1^{-2}17a_1) - 0.42(2b_1^{-2}12a_1) + 0.36(2b_1^{-2}16a_1)$
6	21.5	0.14	“$4a_1^{-1}$(mo′)”	0.04				
7	22.7	0.97	“$4a_1^{-1}$(mo′)”	0.95	23.00–23.88 (state 4)[c]	23.62	0.118	$0.34(\underline{4a_1^{-1}}) - 0.51(2b_1^{-2}17a_1) - 0.34(2b_1^{-2}13a_1)$
8	24.4	1.01	$D3'$	0.89	26.9[b]	27.33	0.020	$0.40(2b_1^{-2}13a_1) - 0.36(5a_1^{-1}8b_22b_2^{-1}) - 0.33(2b_1^{-1}3a_22b_2^{-1})$
					27.9[b]	27.85	0.050	$0.37(2b_2^{-1}6b_25a_1^{-1}) - 0.35(2b_2^{-1}8b_25a_1^{-1}) + 0.30(2b_1^{-1}6b_15a_1^{-1})$
					28.65[b]	28.54	0.019	$0.50(2b_2^{-1}3a_22b_1^{-1}) + 0.39(2b_2^{-1}2a_22b_1^{-1}) + 0.33(5a_1^{-1}6b_12b_1^{-1})$

[a] State-resolved dipole oscillator strengths for the formation of H($2p$) atoms in the photoexcitation of H_2S (present results).

[b] Binding energies measured with the x-ray photoelectron spectroscopy [36].

[c] Binding energies measured with the He II photoelectron spectroscopy [57]. The labels are the same as those by Baltzer *et al.* [57] and identify the ionic states in Fig. 11(b).

[d] Results calculated with the SAC-CI general-R method [53]. Only the states below 29 eV with the monopole intensities higher than ~0.02 are shown.

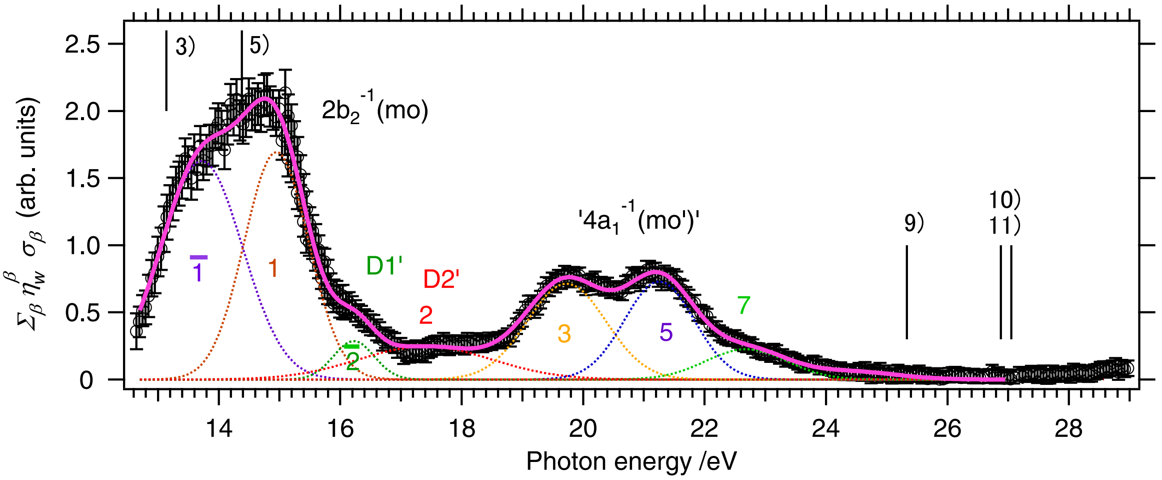

FIG. 12. The sum of the sensitivity-weighted cross sections for the S* fluorescences $\sum_\beta \eta_w^\beta \sigma_\beta(E)$ as a function of incident photon energy in the photoexcitation of H_2S. The curves show the best result of the fitting of the first term in Eq. (16) (dotted curve: peak originating from superexcited state s, solid curve: the sum of them). The superexcited states involved are summarized in Table V.

doubly excited states. The quotation marks again show that they are multiconfiguration states due to the electron correlation. The doubly excited states responsible for the sharp peaks in Fig. 11(a) ($s = 4, 6$) are likely to be built on the ion-core state 3, since the ion-core state 3 shows a clear vibrational progression in the photoelectron spectrum [57] measured with the much higher energy resolution than in Fig. 11(b). The peaks ($s = 4, 6$) would probably be single vibrational peaks.

In the range above the "$4a_1^{-1}$(mo′)" states there exists a superexcited state at 24.4 eV ($s = 8$), which is likely to be built on one of the ion-core states in the range above the "$4a_1^{-1}$" states of H_2S^+ [36,58], probably the ion-core state at 26.9 eV [36]. Those ion-core states are expressed as the superpositions of the double-hole one-electron configurations with negligible contributions of single-hole configurations (see Table V). It is hence concluded that the superexcited state at 24.4 eV ($s = 8$) is a doubly excited state with negligible contributions of singly excited configurations and is referred to as the $D3'$ state. The existence of the $D3'$ state seems not to be certain because no discernible peak appears around 24 eV in Fig. 11(a). However, the contribution of the dissociative autoionization from the $D3'$ state was clearly seen in the cross section curve for the formation of energetic H^+ ions in the photoionization of H_2S [59].

Table V summarizes the above-mentioned discussion about the superexcited states involved in Figs. 11(a) and 12, and the arrows in Fig. 11 connect the superexcited states and their ion-core states. As seen in Table V, ten superexcited states of H_2S have been found in the present experiment ($s = 1$–8 and $s = \bar{1}, \bar{2}$), two of which are singly excited $2b_2^{-1}$(mo) states and the others are doubly excited $D1'$, $D2'$, "$4a_1^{-1}$(mo′)", and $D3'$ states. The singly excited $2b_2^{-1}$(mo) states are single-configuration states and doubly excited states are multiconfiguration states.

Diercksen and Langhoff [60] calculated the state-resolved DOSs for the photoabsorption of H_2S in the outer and inner valence range with the single- and coupled-channel static exchange approximations. The calculated energy positions of the $2b_2^{-1}$(mo) states are within the $2b_2^{-1}$(mo) peak at 13.7 eV in Fig. 12 ($s = \bar{1}$ peak). The calculated energies of the $4a_1^{-1}$(mo′) states, however, do not account for the "$4a_1^{-1}$(mo′)" peaks in Figs. 11(a) and 12.

The superexcited states of H_2S were studied with detecting fluorescence photons from H, S, S^+, S^{2+}, SH, and SH^+ fragments in the range of S $2p$ excitation [61,62]. It is remarkable that the bands in the Lyman-α, Balmer-α, and Balmer-β cross section curves around the S $2p$ ionization limit [62] show a shape similar to the inner valence band in the Lyman-α cross section curve in Fig. 11(a) (see Fig. 13). This fact indicates that similar excited orbitals are involved in the inner valence and inner shell ranges. This similarity in band shapes between the inner valence and inner shell ranges is also seen in H_2O as mentioned in Sec. IV A (see Fig. 10).

Thanks to the cross sections on the absolute scale in Fig. 11(a), state-resolved DOSs for the formation of H($2p$) atoms in the photoexcitation of H_2S are obtained following Eq. (15) and are summarized in Table V. They are displayed in Fig. 9(c) in the manner of the DOS pattern for H($2p$) formation. In Fig. 9(d) the experimental photoelectron spectra and calculated monopole intensities in Fig. 11(b) are displayed again to show the ionic states on which the precursor superexcited states of H($2p$) atoms are built.

Figures 9(a) and 9(c) are significant results of the present experiment showing the absolute values of the state-resolved DOSs for the formation of H($2p$) atoms in the photoexcitation of H_2O and H_2S. The DOS patterns for H($2p$) formation from H_2O and H_2S in the inner valence range are more complex than those in the outer valence range. This complexity originates from the appearance of the doubly excited states with considerable magnitudes of the DOSs, which appearance is due to the stronger electron correlation in the inner valence range than that in the outer valence range. In the next subsection we compare the DOS patterns for H($2p$) formation from H_2O and H_2S.

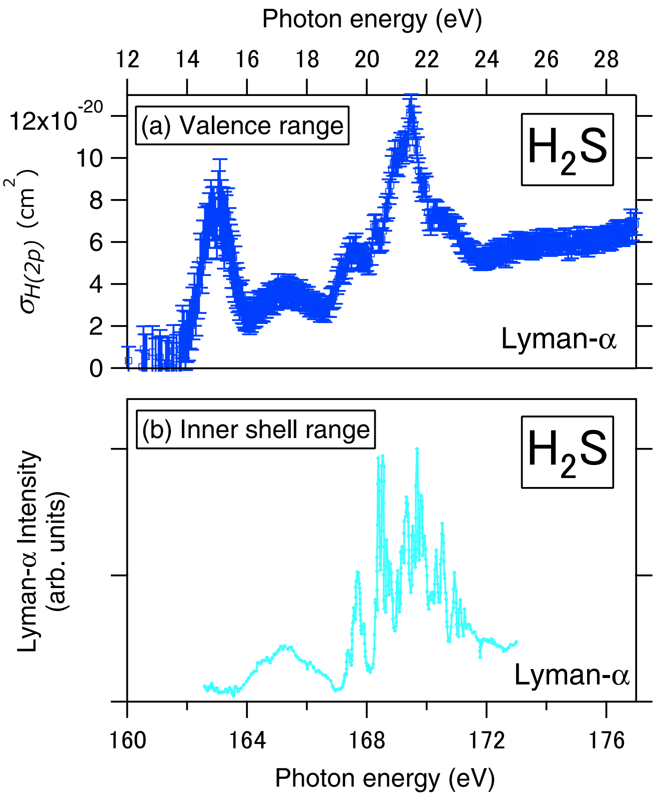

FIG. 13. (a) Cross sections for H($2p$) formation in the photoexcitation of H_2S in the outer and inner valence range recorded with the energy resolution of 50 meV at 21 eV photon energy, which cross sections are the same as in Fig. 11(a). (b) Cross sections for Lyman-α fluorescence emission in the photoexcitation of H_2S in the S $2p$ inner shell range recorded with the energy resolution of about 25 meV (Fig. 3 in Ref. [62]).

C. Comparison between H_2O and H_2S

Before the comparison in terms of the DOS patterns we note that the major fragment atoms are changed with going from H_2O to H_2S. The superexcited H_2O molecules in the valence range leads to H($2p$) formation but do not lead to the formation of O* atoms such as O*($2p^{-1}3s\ {}^3S^o$) atoms emitting the 130 nm fluorescence line quite so much that the photon signal in the nondispersed fluorescence experiments is dominated by the Lyman-α fluorescence as mentioned in Sec. II B 1. On the other hand, the superexcited H_2S molecules in the valence range lead to the formation of H($2p$) and S*($3p^{-1}4s$) atoms as shown in Fig. 2, and the latter fragments are more abundant. The wider range of fragment atoms in H_2S is accounted for by the denser population of the potential energy surfaces of H_2S in the valence range since the denser population enhances the nonadiabatic transitions between the superexcited states of H_2S.

There is also a possibility that the spin-orbit interaction brings about the change of the main-fragment atoms in H_2S. In this respect it is remarkable that S($3p^{-1}4s\ {}^3D^o$) atoms are produced from H_2S molecules in the singlet superexcited $2b_2^{-1}$(mo) states ($s = 1, \bar{1}$) through a two-body dissociation process, i.e., S($3p^{-1}4s\ {}^3D^o$) + $H_2(X\ {}^1\Sigma_g^+)$, as seen in the second panel of Fig. 3 and the dissociation limit 1 in Table III. Only the triplet state of an H_2S molecule arises from the triplet state of an S atom and singlet state of an H_2 molecule. It follows that the spin-orbit interaction in the superexcited states of H_2S in the valence range is so strong that the photoexcited H_2S in the singlet $2b_2^{-1}$(mo) states transfers to the triplet states correlating to S($3p^{-1}4s\ {}^3D^o$) + $H_2(X\ {}^1\Sigma_g^+)$ through the spin-orbit interaction. Such nonadiabatic transitions seem less likely in the superexcited states of H_2O composed of a lighter oxygen atom.

We then compare the DOS patterns of H_2O and H_2S in terms of the magnitudes of the DOSs and energies of the superexcited states. The DOSs for the formation of H($2p$) atoms are $\sim 10^{-3}$ in the photoexcitation of H_2S and the sum of all is 5.67×10^{-3} (see Table V) while those for the formation of H($2p$) atoms range from $\sim 10^{-3}$ to $\sim 10^{-2}$ in the photoexcitation of H_2O and the sum of all is 32.4×10^{-3} (see Table IV). Focusing on the doubly excited states, the formation of H($2p$) atoms is also suppressed in the photoexcitation of H_2S: $\Sigma_s f^s_{\mathrm{H}(2p)} = 4.79 \times 10^{-3}$ in H_2S vs $\Sigma_s f^s_{\mathrm{H}(2p)} = 8.60 \times 10^{-3}$ in H_2O. The suppression of H($2p$) formation seems to be closely related to the change of the major fragment atoms mentioned above.

There exists a large difference between the "$2a_1^{-1}$(mo′)" peak in H_2O and the "$4a_1^{-1}$(mo′)" peaks in H_2S as seen in Figs. 9(a) and 9(c): just one "$2a_1^{-1}$(mo′)" state is responsible for H($2p$) formation in H_2O while three well-separated "$4a_1^{-1}$(mo′)" states (s = 3, 5, 7 in Table V) are responsible for H($2p$) formation in H_2S. The relation between the $2a_1$ orbital in H_2O and the $4a_1$ orbital in H_2S is seen in the beginning of Sec. IV. This difference is explained as follows. As seen in Figs. 9(b) and 9(d) the inner valence band of the experimental photoelectron spectrum of H_2S is more complex than that of H_2O, which is in accordance with the theoretical prediction [53]: the calculated splitting of the "$2a_1^{-1}$" states of H_2O^+ is just 290 meV, whereas the splitting of the "$4a_1^{-1}$" states of H_2S^+ amounts to 1.4 eV [see the red vertical bars in Figs. 9(b) and 9(d)]. It is thus concluded from the much smaller splitting of the "$2a_1^{-1}$" ion-core states of H_2O^+ that just one "$2a_1^{-1}$(mo′)" peak is apparently observed, i.e., the "$2a_1^{-1}$(mo′)" peak would in fact be comprised of two peaks that are closely located. On the other hand the enhancement of the splitting of the "$4a_1^{-1}$" ion-core states of H_2S^+ results in the appearance of the three well-separated "$4a_1^{-1}$(mo′)" peaks. The close relation between the doubly excited states and their ion-core states shows that electrons in the excited orbitals denoted by mo′ in Fig. 9 are weakly bound by ion cores. The enhanced splitting of the doubly excited "$4a_1^{-1}$(mo′)" states of H_2S in comparison with that of the "$2a_1^{-1}$(mo′)" states of H_2O, i.e., 3.0 eV for H_2S (see Table V) vs much smaller than 1 eV for H_2O, originates from the enhancement of the electron correlation with going from H_2O to H_2S. This is consistent with the fact that the $2b_2^{-1}$(mo) state of H_2S is much closer to the doubly excited states of H_2S than the $1b_2^{-1}$(mo) state of H_2O is, as seen in Figs. 9(a) and 9(c). The border between the inner valence and outer valence ranges becomes obscure with going from H_2O to H_2S.

V. CONCLUSION

The superexcited states of H_2S have been studied in detail with determining the cross sections for the formation of H(2p) atoms on the absolute scale against the incident photon energy in the outer and inner valence range. This method is useful for extracting the discrete electronic state from the superposition with the continuous electronic states. Ten superexcited states have been found. Two of them in the range 13–15 eV are singly excited $2b_2^{-1}$(mo) states with a single configuration while the other eight states in the range 16–25 eV are doubly excited states with multiple configurations (see Table V). The state-resolved dipole oscillator strengths for H(2p) formation in H_2S have been obtained: they are $\sim 10^{-3}$.

Almost the same experiments have been carried out for H_2O, complementary to the early experiments for H_2O by our group [20]. The state-resolved dipole oscillator strengths for H(2p) formation range from $\sim 10^{-3}$ to $\sim 10^{-2}$ in H_2O. It is found that the major fragment atoms are changed from H(2p) atoms to excited central atoms with going from the photoexcitation of H_2O to that of H_2S.

The superexcited states of H_2O and H_2S are compared based on the similarity and difference of the electronic structures: both molecules have C_{2v} symmetry in their ground electronic states and have eight valence electrons, whereas the densities of the superexcited states in H_2S are higher than those in H_2O.

It has turned out from the comparison that (i) the smaller values of the dipole oscillator strengths for H(2p) formation in the photoexcitation of H_2S seem to be related to the change of the major fragment atoms, (ii) the energy splitting of the doubly excited "$4a_1^{-1}$(mo′)" states of H_2S is enhanced in comparison with that of the doubly excited "$2a_1^{-1}$(mo′)" states of H_2O, i.e., 3.0 eV for H_2S vs much smaller than 1 eV for H_2O, and the enhancement is caused by the increased electron correlation in H_2S due to the higher density of the superexcited states in H_2S than in H_2O, and (iii) the border between the inner valence and outer valence ranges becomes more obscure in H_2S than in H_2O.

Interestingly the H^* fluorescence cross section curves around the O 1s shake-up limit for H_2O [55] and around the S 2p ionization limit for H_2S [62] show the bands similar to the inner valence bands in the cross section curves for H(2p) formation in the photoexcitation of H_2O and H_2S. This similarity between the inner valence band and inner shell band in shape indicates that the electrons are excited to similar orbitals from the valence orbitals or inner shell orbitals, resulting in the similar shapes of the potential energy surfaces of the superexcited states.

ACKNOWLEDGMENTS

This work has been carried out under the approval of Photon Factory Program Advisory Committee for Proposal No. 2016G001, and BESSY II for Proposal No. 16204174-ST/R. The work was supported by the Deutsche Forschungsgemeinschaft DFG via the FOR 1789 and the project ELCH of the state Hesse Landes-Offensive zur Entwicklung Wissenschaftlich-okonomischer Exzellenz (LOEWE).

---

[1] H. Nakamura, Int. Rev. Phys. Chem. **10**, 123 (1991).

[2] Y. Hatano, Phys. Rep. **313**, 109 (1999).

[3] J. N. Bardsley, J. Phys. B **1**, 349 (1968).

[4] I. Sánchez and F. Martín, Phys. Rev. A **57**, 1006 (1998).

[5] F. Martín, J. Fernández, T. Havermeier, L. Foucar, Th. Weber, K. Kreidi, M. Schöffler, L. Schmidt, T. Jahnke, O. Jagutzki, A. Czasch, E. P. Benis, T. Osipov, A. L. Landers, A. Belkacem, M. H. Prior, H. Schmidt-Böcking, C. L. Cocke, and R. Dörner, Science **315**, 629 (2007).

[6] D. Dowek, J. F. Pérez-Torres, Y. J. Picard, P. Billaud, C. Elkharrat, J. C. Houver, J. L. Sanz-Vicario, and F. Martín, Phys. Rev. Lett. **104**, 233003 (2010).

[7] J. E. Furst, T. J. Gay, J. Machacek, D. Kilkoyne, and K. W. McLaughlin, Phys. Rev. A **86**, 041401(R) (2012).

[8] Y. Nakanishi, K. Hosaka, R. Kougo, T. Odagiri, M. Nakano, Y. Kumagai, K. Shiino, M. Kitajima, and N. Kouchi, Phys. Rev. A **90**, 043405 (2014).

[9] K. Hosaka, K. Shiino, Y. Nakanishi, T. Odagiri, M. Kitajima, and N. Kouchi, Phys. Rev. A **93**, 063423 (2016).

[10] T. Odagiri, M. Murata, M. Kato, and N. Kouchi, J. Phys. B **37**, 3909 (2004).

[11] M. Glass-Maujean *et al.*, J. Phys. B **37**, 2677 (2004).

[12] T. Odagiri, Y. Kumagai, M. Nakano, T. Tanabe, I. H. Suzuki, M. Kitajima, and N. Kouchi, Phys. Rev. A **84**, 053401 (2011).

[13] A. Fischer, A. Sperl, P. Cörlin, M. Schönwald, S. Meuren, J. Ullrich, T. Pfeifer, R. Moshammer, and A. Senftleben, J. Phys. B **47**, 021001 (2014).

[14] K. Hosaka, K. Minamizaki, T. Tsuchida, K. Yachi, T. Odagiri, T. Maeda, M. Kitajima, and N. Kouchi, Phys. Rev. A **96**, 012706 (2017).

[15] M. Kato, K. Kameta, T. Odagiri, N. Kouchi, and Y. Hatano, J. Phys. B **35**, 4383 (2002).

[16] M. Kato, T. Odagiri, K. Kameta, N. Kouchi, and Y. Hatano, J. Phys. B **36**, 3541 (2003).

[17] M. Kato, T. Odagiri, K. Kodama, M. Murata, K. Kameta, and N. Kouchi, J. Phys. B **37**, 3127 (2004).

[18] H. Fukuzawa, T. Odagiri, T. Nakazato, M. Murata, H. Miyagi, and N. Kouchi, J. Phys. B **38**, 565 (2005).

[19] L. Ishikawa, T. Odagiri, K. Yachi, T. Nakazato, M. Kurokawa, M. Kitajima, and N. Kouchi, J. Phys. B **41**, 195204 (2008).

[20] M. Nakano, T. Odagiri, T. Tanabe, K. Funatsu, I. H. Suzuki, M. Kitajima, and N. Kouchi, J. Phys. B **43**, 215206 (2010).

[21] A. Hans, A. Knie, Ph. Schmidt, L. Ben Ltaief, C. Ozga, Ph. Reiß, H. Huckfeldt, M. Forstel, U. Hergenhahn, and A. Ehresmann, Phys. Rev. A **92**, 032511 (2015).

[22] E. M. García, J. Álvarez Ruiz, S. Menmuir, E. Rachlew, P. Erman, A. Kivimäki, M. Glass-Maujean, R. Richter, and M. Coreno, J. Phys. B **39**, 205 (2006).

[23] J. R. Machacek, V. M. Andrianarijaona, J. E. Furst, A. L. D. Kilcoyne, A. L. Landers, E. T. Litaker, K. W. McLaughlin, and T. J. Gay, J. Phys. B **44**, 045201 (2011).

[24] M. Murata, T. Odagiri, and N. Kouchi, J. Phys. B **39**, 1285 (2006).

[25] T. Odagiri, H. Miyagi, M. Murata, H. Fukuzawa, M. Kurokawa, M. Kitajima, and N. Kouchi, J. Phys. B **42**, 055101 (2009).

[26] T. Odagiri, K. Funatsu, T. Tanabe, I. H. Suzuki, M. Kitajima, and N. Kouchi, J. Phys. B **42**, 225101 (2009).

[27] T. Tsuchida, T. Odagiri, L. Ishikawa, K. Yachi, K. Shigemura, N. Ohno, K. Hosaka, M. Kitajima, and N. Kouchi, J. Phys. B **44**, 175207 (2011).

[28] H. Liebel, S. Lauer, F. Vollweiler, R. Müller-Albrecht, A. Ehresmann, H. Schmoranzer, G. Mentzel, K.-H. Schartner, and O. Wilhelmi, Phys. Lett. A **267**, 357 (2000).

[29] H. Schmoranzer, H. Liebel, F. Vollweiler, R. Müller-Albrecht, A. Ehresmann, K.-H. Schartner, and B. Zimmermann, Nucl. Instrum. Methods A **467-468**, 1526 (2001).

[30] M. Glass-Maujean, Ch. Jungen, H. Schmoranzer, A. Knie, I. Haar, R. Hentges, W. Kielich, K. Jänkälä, and A. Ehresmann, Phys. Rev. Lett. **104**, 183002 (2010).

[31] U. Fano, Phys. Rev. **124**, 1866 (1961).

[32] K. Siegbahn, C. Nordling, G. Johansson, J. Hedman, P. F. Heden, K. Hamrin, U. Gelius, T. Bergmark, L. O. Werme, R. Manne, and Y. Baer, *ESCA Applied to Free Molecules* (North-Holland, Amsterdam, 1969).

[33] W. F. Chan, G. Cooper, and C. E. Brion, Chem. Phys. **178**, 387 (1993).

[34] R. Feng, G. Cooper, and C. E. Brion, Chem. Phys. **244**, 127 (1999).

[35] M. S. Banna, H. McQuaide, R. Malutzki, and V. Schmidt, J. Chem. Phys. **84**, 4739 (1986).

[36] M. Y. Adam, A. Naves de Brito, M. P. Keane, S. Svensson, L. Karlsson, E. Kiillne, and N. Correia, J. Electron Spectrosc. Relat. Phenom. **56**, 241 (1991).

[37] Ph. V. Demekhin, I. D. Petrov, V. L. Sukhorukov, W. Kielich, A. Knie, H. Schmoranzer, and A. Ehresmann, Phys. Rev. Lett. **104**, 243001 (2010).

[38] A. Hans, P. Schmidt, C. Ozga, G. Hartmann, X. Holzapfel, A. Ehresmann, and A. Knie, Materials **11**, 869 (2018).

[39] G. Reichardt, J. Bahrdt, J.-S. Schmidt, W. Gudat, A. Ehresmann, R. Müller-Albrecht, H. Molter, H. Schmoranzer, M. Martins, N. Schwentner, and S. Sasaki, Nucl. Instrum. Methods Phys. Res. Sect. A **467**, 462 (2001).

[40] K. Ito, Y. Morioka, M. Ukai, N. Kouchi, Y. Hatano, and T. Hayaishi, Rev. Sci. Instrum. **66**, 2119 (1995).

[41] Y. Kumagai, T. Odagiri, M. Nakano, T. Tanabe, I. H. Suzuki, K. Hosaka, M. Kitajima, and N. Kouchi, J. Chem. Phys. **139**, 164307 (2013).

[42] M. Glass-Maujean and H. Schmoranzer, J. Phys. B **38**, 1093 (2005).

[43] Model F4655-10, Hamamatsu Photonics.

[44] C. Martin and S. Bowyer, Appl. Opt. **21**, 4206 (1982).

[45] S. J. Brotton, E. Vyskocil, W. Kedzierski, and J. W. McConkey, Phys. Rev. A **79**, 042709 (2009).

[46] NIST Atomic Spectra Database, https://www.nist.gov/pml/atomic-spectra-database.

[47] L. R. Peebles and P. Marshall, J. Chem. Phys. **117**, 3132 (2002).

[48] K. P. Huber and G. Herzberg, *Molecular Spectra and Molecular Structure: IV. Constants of Diatomic Molecules* (Van Nostrand-Reinhold, New York, 1979).

[49] G. Herzberg, *Molecular Spectra and Molecular Structure: III. Electronic Spectra and Electronic Structure of Polyatomic Molecules* (Van Nostrand-Reinhold, Princeton, NJ, 1967).

[50] N. Kouchi and T. Odagiri, *Charged Particle and Photon Interactions with Matter, Chemical, Physiochemical, and Biological Consequences with Applications*, edited by A. Mozumder and Y. Hatano (Marcel Dekker, New York, 2004), Chap. 5.

[51] R. Schinke, *Cambridge Monographs on Atomic, Molecular and Chemical Physics: 1. Photodissociation Dynamics* (Cambridge University Press, Cambridge, 1993), pp. 115–120.

[52] H. Nakamura, J. Phys. Soc. Jpn. **26**, 1473 (1969).

[53] M. Ehara, M. Ishida, and H. Nakatsuji, J. Chem. Phys. **114**, 8990 (2001).

[54] L. C. Lee, X. Wang, and M. Suto, J. Chem. Phys. **86**, 4353 (1987).

[55] A. Kivimäki, M. de Simone, M. Coreno, V. Feyer, E. M. García, J. A. Ruiz, R. Richter, and K. C. Prince, Phys. Rev. A **75**, 014503 (2007).

[56] R. Feng, G. Cooper, and C. E. Brion, Chem. Phys. **249**, 223 (1999).

[57] P. Baltzer, L. Karlsson, M. Lundqvist, B. Wannberg, D. M. P. Holland, and M. A. MacDonald, Chem. Phys. **195**, 403 (1995).

[58] M. Y. Adam, C. Cauletti, and M. N. Piancastelli, J. Electron Spectrosc. Relat. Phenom. **42**, 1 (1987).

[59] K. F. Dunn, R. Browning, M. A. MacDonald, C. R. Browned, and C. J. Latimer, J. Phys. B **31**, 4173 (1998).

[60] G. H. F. Diercksen and P. W. Langhoff, Chem. Phys. **112**, 227 (1987).

[61] M. Meyer, P. O'Keeffe, J. Plenge, R. Flesch, and E. Rühl, J. Chem. Phys. **125**, 214306 (2006).

[62] G. Vall-llosera, E. Melero García, A. Kivimäki, E. Rachlew, M. Coreno, M. de Simone, R. Richter, and K. C. Prince, Phys. Chem. Chem. Phys. **9**, 389 (2007).